THE CHARACTERISTICS OF DUST PARTICLES DETECTED BY CASSINI NEAR SATURN'S RING PLANE

by

Zhenzhen Wang

A thesis submitted in partial fulfillment
of the requirements for the Doctor of
Philosophy degree in Physics
in the Graduate College of
The University of Iowa

July 2006

Thesis Supervisor: Professor Donald A. Gurnett

Graduate College
The University of Iowa
Iowa City, Iowa

CERTIFICATE OF APPROVAL

PH.D. THESIS

This is to certify that the Ph.D. thesis of

Zhenzhen Wang

has been approved by the Examining Committee for the thesis requirement for the Doctor of Philosophy degree in Physics at the July 2006 graduation.

Thesis Committee: ______________________________
Donald A. Gurnett, Thesis Supervisor

____
Kenneth Gayley

____
Robert Merlino

____
Steven Spangler

____
Robert Yager

ACKNOWLEDGMENTS

There are quite a number of people who help me to get to this point in my life. I would like to take this opportunity to express my gratitude to all of them. Foremost is my advisor, Prof. Donald A. Gurnett. I wish to acknowledge his foresight in suggesting the topic, which has been both interesting and rewarding. I also thank him for his support and advice throughout. Thanks also go to Prof. Steven R. Spangler, who advised me on the last part of this project and gave me much support.

Special thanks go to William S. Kurth and Terrance F. Averkamp. Thanks them for reading the thesis and giving me valuable comments. Terry also gave me a lot of help on programming. I would also like to thank Ann Persoon for her wonderful job on figure processing and Kathy Kurth for helping me to format the thesis. Thanks also go to all members in space plasma group, a wonderful team in the Univ. of Iowa. Working with them has been an inspiring and enjoyable learning experience.

I am most grateful to my parents who have always been kind, patient, loving and understanding. They have been always encouraging and supportive.

Although they are not directly associated with this project, I also wish to acknowledge the many friends, who have helped me in various ways always.

This research was supported by NASA through contract 127993 with the Jet Propulsion Laboratory.

ABSTRACT

This thesis analyzes the dust impacts detected by the Radio and Plasma Wave Science (RPWS) instrument on the Cassini spacecraft during the inbound and outbound passes through Saturn's ring plane at 2.634 and 2.630 Saturn radii on July 1, 2004. When a small particle strikes the spacecraft at a high velocity, it is instantly vaporized and produces a small cloud of plasma that expands radially outward from the impact site. As the plasma cloud expands it produces a voltage pulse on the RPWS electric field antennas, the amplitude of which is proportional to the mass of the impacting particle. The impact rate at both ring plane crossings provides a good fit to the sum of two Gaussians, with a peak impact rate of about 1200 to 1500 impacts per second (the exact value depends on the voltage threshold used), and a north-south thickness of about 300 km. From the impact rate, effective cross-sectional area, and the relative velocity of the spacecraft, the number density of the impacting particles can be calculated and is estimated to be about 6×10^{-3} m^{-3}. The mass distribution depends on the distance from the ring plane, and varies from about m^{-2} near the ring plane, at $z = 0 \pm 100$ km, where z is the north-south distance from the ring plane, to as steep as m^{-4} well away from the ring plane, at $z = 500 \pm 100$ km. The mechanisms involved in the impact detection are discussed and a formula relating the root-mean-square particle mass to the root-mean-square voltage on the antenna is derived. Using this formula, the root-mean-square mass is estimated to be 7.7×10^{-11} grams, which for water ice particles with a density of 0.92 g cm^{-3} gives a root-mean-square radius of about 2.6 μm. To facilitate possible comparisons with optical observations, we have computed the expected optical depth and angular

distribution of scattered light using the measured dust parameters. The optical depth normal to the ring plane at 500 nm is estimated to be about 4.26×10^{-8}, and the full width at half maximum (FWHM) of the forward scattered light is estimated to be 9°.

TABLE OF CONTENTS

LIST OF FIGURES

CHAPTER I

INTRODUCTION

It is well known that there are a large number of very small dust particles with sizes on the order of a few microns in the Saturn system [Smith *et al.*, 1981; Esposito *et al.*, 1984]. These very small particles are primarily centered near the ring plane at a radial distance near and inside the G ring, and are most likely produced by micrometeoroid impacts on the rings and icy moons. The first direct detection of these small dust particles was with the radio and plasma wave instrument on the Voyager 2 spacecraft. During the Voyager 2 flyby of Saturn, numerous impulsive signals were detected both by the plasma wave and the planetary radio astronomy instruments as the spacecraft crossed the ring plane at a radial distance of 2.88 R_S (R_S = 60,268 km) slightly outside of the G ring [Scarf *et al.*, 1982; Warwick *et al.*, 1982]. At peak intensity the spectrum of this impulsive noise extended from frequencies of 10 Hz or less to approximately 1 MHz, which is well above the local electron plasma frequency. Because the spectrum extended well above the electron plasma frequency, which is the highest characteristic frequency of the plasma, it was concluded that this noise could not be due to plasma waves. From the impulsive waveform and the close proximity to the ring plane, Scarf *et al.* [1982] and Warwick *et al.* [1982] concluded that the noise was produced by the impacts of micron-sized particles hitting the spacecraft.

The mechanisms involved in the coupling of the impacts to the plasma wave instrument (PWS) were discussed in detail by Gurnett *et al.* [1983]. The plasma wave instrument on the Voyager 2 spacecraft used two antenna elements as a dipole. Based on the assumptions about the charge yield of the impacts and the coupling efficiency of the released charge to the antenna elements, Gurnett *et al.* provided an initial estimate of the mass and size distribution of the dust particles. A critical parameter α, called collection coefficient, was introduced to measure the ratio of the charge collected by the antenna to the total released charge. However the collection coefficient depends on the potential of the antenna as well as other unknown factors such as the location of the impact, so it was very difficult to estimate the size of the particles from fundamental principles.

Aubier *et al.* [1983] discussed the mechanisms involved in the impulsive noise spectrum detected by the planetary radio astronomy instrument (PRA) on Voyager 2, which used the two antenna elements as two independent monopoles. Based on the assumption that the induced voltage between the antenna and the spacecraft body is related to the electric field in the expanded ionized cloud, the impulsive noise spectrum was modeled in the time domain. After Fourier transforming, the voltage spectrum was found to be proportional to f^{-4}, which is consistent with the experimentally observed relationship between the voltage spectral density and the frequency of the noise [Meyer-Vernet *et al.*, 1986]. If all of the particles were to have the same size, a quantitative approach of this process gave an estimation of the dust particle size of about 2.3 μm [Aubier *et al.*, 1983].

The objective of my Ph.D thesis is to use data from the Radio and Plasma Wave Science instrumentation (RPWS) on the Cassini spacecraft to investigate dust impacts during the inbound and outbound passes through the rings of Saturn, which occurred on

July 1st, 2004. After the impact, the escaping electrons cause an electric field to develop in the plasma cloud between the spacecraft body and the escaping electrons. It is this polarization electric field that induces voltage pulses in the electric antennas. By counting the voltage pulses a very accurate measurement of the impact rate can be obtained. Knowing the relative velocity between the spacecraft and the dust particles, which are assumed to be in circular orbits around Saturn, and the cross-sectional area of the spacecraft, the number density of the impacting particles will be determined. Using the theory developed by Aubier *et al.* [1983] the root-mean-square mass and size distribution of dust particles will also be determined. At present there are no observations of scattered light from the region of the ring where these measurements were made. In order to facilitate possible future comparisons with optical remote sensing measurements the optical depth and angular distribution of scattered sunlight will be determined.

CHAPTER II

THE CASSINI MISSION

The Cassini spacecraft, which was designed to investigate Saturn and its rings, moons and magnetosphere, was launched on October 15th, 1997, and placed in orbit around Saturn on July 1st, 2004. Figure 1 shows the trajectory of the Cassini spacecraft during the first encounter with Saturn. The spacecraft passed northbound through the ring plane between the F and G rings on the inbound pass and southbound between the same two rings on the outbound pass. The inbound ring plane crossing occurred at 00:46:31 Universal Time (UT) and a radial distance of 2.634 R_S (R_S = 60,268 km). The outbound ring plane crossing occurred at 04:33:51 UT and a radial distance of 2.630 R_S. Since it is the first orbiter of Saturn, Cassini can provide much better spatial and temporal coverage than Voyagers 1 and 2. Two instruments on Cassini provide measurements of small dust particles: the Cosmic Dust Analyzer (CDA) and the RPWS. The CDA is specifically designed to detect and analyze small dust particles [Srama *et al.*, 2004], whereas the RPWS is mainly designed to study radio and plasma waves [Gurnett *et al.*, 2004]. Although the CDA has provided very useful surveys of micron and sub-micron dust particles in the outer regions of Saturn's rings [Kempf *et al.*, 2005a; 2005b], during the two very close passages through the rings that occurred on July 1st, 2004, the CDA was not operating. Thus, the RPWS provided the only measurements of dust particles in this crucial region, a region that probably will not be directly sampled again during the Cassini mission.

Compared with the Voyager plasma wave instrumentation, several very significant improvements were made in the Cassini RPWS that significantly enhance the ability to detect and analyze dust impacts. First, the RPWS can operate the antenna elements both as a dipole and as a monopole. With this system, the charge released by the impact can be determined directly from the amplitude of the voltage pulse on the monopole antenna, thereby giving a signal that is proportional to the mass of the impacting dust particle. Second, the dynamic range of the RPWS antenna voltage waveforms was increased from 4-bit resolution to 8-bit, thereby making it possible to obtain mass distributions from pulse height analysis of the observed impact waveforms. In addition, an on-board microprocessor algorithm can be used to continuously identify and analyze dust impacts throughout the mission.

CHAPTER III

THE RPWS INSTRUMENT

RPWS

For a detailed description of the Cassini RPWS investigation, see Gurnett *et al.* [2004]. The RPWS instrumentation consists of three electric antennas, three magnetic antennas, a Langmuir probe and its associated electronics, and five specialized receivers. In the dust detecting task, we only use the high frequency receiver and the wideband receiver.

Figure 2 shows a simplified block diagram of the RPWS instruments. The left column shows the three kinds of RPWS sensors that are used to provide measurements of radio and plasma waves. Three monopole electric field antennas, labeled *E*u, *E*v, and *E*w, are used to provide electric field measurements. The tri-axial search coil magnetic antennas, labeled *B*x, *B*y, and *B*z, are used to detect three orthogonal magnetic components of electromagnetic waves. The spherical Langmuir probe is used to detect electron density and temperature. The locations of the RPWS sensors and their relationship with other structures on the Cassini spacecraft are shown in Figure 3. Both the electric antennas and the Langmuir probe can be used to detect dust impacts.

Through a network of switches in the block labeled “antenna selection switches,” the RPWS antennas can be connected ti various combinations to the five receivers that are shown in the middle column of the block diagram in Figure 2. The high frequency receiver (HFR) provides simultaneous auto- and cross-correlation measurements from two selected antennas over a frequency range from 3.5 kHz to 16 MHz. The medium frequency receiver (MFR) and the low frequency receiver (LFR) provide intensity measurements from a single selected antenna over a frequency range from 24 Hz to 12 kHz and from 1 to 26 Hz, respectively. The sounder transmitter is used to transmit short square wave pulses from 3.6 to 115.2 kHz. It can also provide a direct measurement of the electron number density by exciting resonances in the plasma. The five-channel waveform receiver (WFR) is used to collect simultaneous waveforms from up to five sensors for short intervals over a frequency range from 1 to 26 Hz or from 3 Hz to 2.5 kHz. The wideband receiver provides nearly continuous wideband waveform measurements in one or two bandwidths, either 60 Hz to 10.5 kHz, or 800 Hz to 75 kHz. In order to obtain the current-voltage characteristics of the probe and thereby the electron density and temperature, the Langmuir probe controller is designed to sweep the bias voltage of the probe over a range from –32 V to +32 V.

Following the receivers, the RPWS data processing unit is shown on the right column of the block diagram. The data processing unit consists of three processors. The low-rate processor controls all instrument functions, collects data from three frequency receivers and the Langmuir probe, and handles all communications with the spacecraft command and data system (CDS). The high-rate processor collects data from the wideband and five-channel waveform receivers and transmits the data to the CDS through the low-rate processor. The data compression processor compresses received data and performs some specialized operations such as on-board dust detection by using waveforms from the wideband receiver.

In the following, we describe the three electric antennas, the low rates spectrum analyzer and the wideband waveform receiver, all of which are used to analyze dust impacts.

Electric Antennas

The RPWS uses three 10m long antenna elements, which extend radially outward from the RPWS antenna bracket located about 1.1 m below the magnetometer boom. The physical orientations of the three elements with respect to the *x*, *y*, and *z* axes of the Cassini spacecraft are shown in Figure 3. The two upper elements, labeled E_U and E_V , are mounted symmetrically at angles of 60 degrees with respect to the *y*-*z* plane of the Cassini spacecraft and form a dipole antenna called E_X . The third antenna, labeled E_w , is rotated at an angle of 37 degrees with respect to the *z* axis of the Cassini spacecraft and is perpendicular to the plane formed by the E_U and E_V elements.

The three electric monopole antennas and their deployment mechanisms were provided by Orbital Sciences Corporation. Physically the antenna elements consist of conducting cylinders, which are formed by two opposing semi-cylindrical strips with interlocking tabs. Each antenna element is 10 m long and 2.86 cm in diameter. The elements are made of beryllium-copper alloy and have a thermal finish of bright polished silver plate externally and black thermal paint internally. Approximately 12% of the surface area is perforated with small holes allowing solar radiation to shine through and heat the shaded side of the element in order to lower the temperature differential across the element and thereby reduce thermally induced bending. At the base of each antenna element spring loaded guide rollers contact the element as it enters the deployment mechanism. These rollers supply a spring constant for small movements of the antenna and are intended to eliminate mechanical deadband of the antenna for the purposes of improving the performance of the attitude control system. A motor-driven deployment mechanism feeds the element through a forming channel that expands the strips into a cylindrical tube. A photograph of the three electric monopole antennas and their deployment mechanisms is shown in Figure 3.

Spectrum Analyzer

The low rate spectrum analyzer, which is used for dust detection consists of the high frequency receiver (HFR) and the medium frequency receiver (MFR). The high frequency receiver provides simultaneous auto- measurement from two selected antennas over a frequency range from 3.5 kHz to 16 MHz. The medium frequency receiver provides intensity measurements from a single selected antenna over a frequency range from 24 Hz to 12 kHz.

The high frequency receiver includes its own digital signal processing unit, therefore being controlled independently by its own processor. All of the receiver parameters can be selected by command, making the high frequency receiver to be operated extremely flexibly. This flexibility allows for regular surveys of the radio frequency spectrum of Saturn at low data rates (typically about 450 bps). For the dust impact detection, the medium frequency receiver can process signals from the E_W antenna, which provides continuous spectral measurements over a frequency range from 24 Hz to 12 kHz, with moderate frequency and temporal resolution and a relatively low data rate. The dynamic range of the medium frequency receiver, from the lowest signal that can be detected to the saturation level, is about 110 dB.

Wideband Waveform Receiver

The purpose of the wideband receiver is to provide high-resolution waveforms of radio emission and plasma waves. The wideband receiver design is based on similar wideband receivers previously used on the Voyager, Galileo, Polar, and Cluster spacecraft [Gurnett *et al.*, 1978, 1992, 1995]. The wideband waveform receiver can process signals from a selected single sensor of E_U, E_V, E_X, E_W, B_X, or Langmuir probe, which provides high-resolution electric and magnetic field waveform measurements over a frequency range from 60 Hz to 10.5 kHz, or 0.8–75 kHz. The wideband waveform receiver can also serve as the front end for the on-board dust detection algorithm. By connecting the wideband receiver to the frequency conversion output of the high frequency receiver, the wideband receiver can also obtain waveforms at higher frequencies. The instantaneous dynamic range of the wideband receiver is 48 dB. To process the expected large dynamic range of the input signals, a set of discrete gain amplifiers and an automatic gain control are used to amplify the signal to the proper level in steps of 10 dB over a range of 0–70 dB, thereby providing a total dynamic range of over 100 dB for the wideband receiver. The output from the discrete gain amplifiers goes to the two bandpass filters, 60 Hz to 10.5 kHz or 0.8–75 kHz, and then the output of the selected bandpass filter is sent to an 8-bit analog-to-digital converter. The sampling rate is 27,777 samples/s for the 10-kHz channel and 222,222 samples/s for the 75-kHz channel. The wideband waveform can be operated in either the temporal domain, or in the frequency domain (Fourier transformed).

CHAPTER IV

OBSERVATIONS

In the mode of operation used for detecting dust impacts during the July 1st, 2004, ring plane crossings, the wideband waveform receiver was configured to respond to the voltage difference between the E_U and E_V antennas (hereafter called the x-axis dipole). At both ring plane crossings very intense impulsive signals were detected in the wideband receiver waveforms, with the maximum intensity occurring very close to the center of the ring plane. Figure 4 shows the wideband voltage waveform obtained during the first ring plane crossing. The sample rate during this pass was such that the time between samples is 36 μs. Some representative dust impact waveforms are shown by the arrows. The dust impact waveforms typically exhibit a very rapid rise on a time scale of a few tens of a microsecond, followed by a complicated recovery waveform. The rise time is controlled by the bandwidth of the receiver, which is 10 kHz. The total duration of the initial pulse typically lasts less than one millisecond, followed by a longer second peak of opposite polarity that lasts for several milliseconds. Most of the pulses fall well within the dynamic range of the receiver. In the gain state that most commonly occurred during the ring plane crossings pulses with an antenna voltage up to about ± 65 mV can be detected. Above this amplitude the pulses are clipped.

To count dust impacts, abrupt steps in the x-axis antenna voltage are identified by requiring that two successive pairs of voltage measurements have slopes of the same sign, either positive or negative. If the total voltage change between the first and last of the three points exceeds 1.6 mV then the step is counted as a dust impact. The 1.6 mV detection threshold was selected on a trial-and-error basis so that it is just above the background noise level at the ring plane crossing. Once an impact is identified, the computer software introduces a dead time of 252 μs ring which no further impacts are recognized. This dead time was introduced to avoid spurious transient effects that are sometimes produced during the complicated recovery waveform. Once the impacts have been identified the impact rate R is computed by counting the number of impacts over a given time interval, after correcting for the dead time. The counting interval is usually about 125 ms, but can vary from as little as 52 ms to as much as 272 ms depending on onboard computer software limitations. The impact rate obtained using this procedure is shown versus time in UT in Figure 5 for the inbound ring plane crossing and in Figure 6 for the outbound ring plane crossing. A scale at the bottom of these figures also shows the z position of the spacecraft measured positive north from the Saturn's equatorial plane. For both ring plane crossings the impact rate reached a maximum value very close to the equator (z = 0) and has a quasi-Gaussian dependence on the distance z from the equatorial plane. As with a similar study of dust impacts by Tsintikidis *et al.* [1994] using the Voyager 2 data, we find that the sum of two Gaussians

$$R = R_0 + R_1 e^{-(z-h)^2/L_1^2} + R_2 e^{-(z-h)^2/L_2^2}, \qquad (1)$$

gives a good fit to the impact rate profile, where h is the offset from the equatorial plane and L is the half thickness of the respective Gaussian component. The optimum values of the fit parameters which are listed in Figures 5 and 6 were obtained by minimizing the goodness of fit parameter $\chi^2 = \Sigma(R_i - R)^2/(N-6)$, where N is the total number of data points and 6 is the number of free parameters in equation (1). The impact rate from the Gaussian fit reaches a maximum value of 1164 s^{-1} for the inbound ring plane crossing and 1262 s^{-1} for the outbound crossing.

The number density, n_0, of the impacting particles can be derived from the impact rate R using the equation

$$R = nUA, \tag{2}$$

where U is the relative speed between the spacecraft and the dust particles and A is the effective cross-sectional area of the spacecraft body. The relative speed between the spacecraft and the particles, which are assumed to be in circular Keplerian orbits around Saturn, was 16.6 km s^{-1} for the inbound ring plane crossing and 15.9 km $s^{-1}$for the outbound ring plane crossing. The spacecraft was oriented during both crossings such that the velocity vector of the arriving dust particles was parallel to spacecraft +Z axis. This orientation was chosen so that the high gain antenna protected the main body of the spacecraft from impacts (see Figure 3). Because of this orientation, the effective area for dust impacts is dominated by the high gain antenna. From the 4 m diameter of the high gain antenna [Matson *et al.*, 2002] the effective cross-sectional area is estimated to be A = 12.6 m^2. Using this area, the relative velocities, and the best fit impact rates at the inbound and outbound ring plane crossing, which are 1164 s^{-1} and 1262 s^{-1}, respectively, the average number densities given by equation (2) at the two ring plane crossings (z = 0) are $n_0 = 5.57 \times 10^{-3}$ m^{-3} and 6.31×10^{-3} m^{-3}, respectively. Recent comparisons with dust measurements in the E ring by the Cassini Cosmic Dust Analyzer (CDA) suggest that the effective area for dust detection by the RPWS maybe significantly smaller than the area of the high gain antenna [Kurth *et al.*, 2006]. If this proves to be correct, then the average number densities computed above will have to be increased by the appropriate factor.

In the Gaussian fit given by equation (1), L_1 gives a measure of the north-south thickness of the "core" dust distribution and L_2 gives a measure of the north-south thickness of the less dense "halo" surrounding the core. For the inbound ring plane crossing, the north-south thickness of the core component, to the e^{-1} points, is 2 L_1 = 296 km and the corresponding north-south thickness of the halo component is 2 L_2 = 714 km. For the outbound ring plane crossing, the north-south thickness of the core is 2 L_1 = 320 km and the thickness of the halo is 2 L_2 = 726 km, both of which are very similar to the inbound crossing.

Since the amplitude of the voltage pulse on the antenna is believed to be proportional to the mass of the impacting particles [Gurnett *et al.*, 1983; Aubier *et al.*, 1983], the mass distribution of the dust particles can be determined from the amplitude distribution of the voltage pulses on antenna. For each impact the maximum voltage amplitude on the x-axis dipole antenna during the 252 μs dead time interval was computed relative to the voltage that existed immediately before the impact. To compute the pulse amplitude distribution, the voltage amplitudes were sorted into the 0.5 mV bins and the number of the impacts in each bin was counted for a specific time interval. By dividing by the total number of impacts, the fraction of impacts per bin, F(V) versus peak voltage of dust impacts can then be obtained. Figure 7 shows F(V) near the center of the first ring plane crossing (–70 km < z < 70 km). Since the pulse amplitude is expected to be proportional to the mass of the impacting particle, this plot gives the mass distribution of the dust particles, dN/dm. The exact voltage-to-mass conversion given at the bottom of the plot will be discussed in the next section. The fractional voltage amplitude distribution in Figure 7 has been plotted on a log-log plot so that a power-law distribution appears as a straight line. As can be seen, above about 1 mV, which is the approximate background noise level, the differential mass distribution dN/dm varies approximately as m^{-2}. Note that some particles almost certainly exist below the detection threshold. Therefore, the number densities described previously only represent a lower limit. To investigate how the mass distribution depends on z the amplitude distribution of the peak voltages observed well away from the center of the first ring plane crossing is shown in Figure 8 for -565 km < z < -425 km, and in Figure 9 for 425 km < z < 565 km. As can be seen the mass distribution away from the ring plane is notably steeper than the mass distribution near the center of the ring plane, varying more like $dN/dm \sim m^{-4}$. The increase in the slope of the mass distribution indicates that there are proportionally fewer large particles in the region well away from the center of the ring plane compared to the region near the center of the ring plane. Another notable feature in Figures 8 and 9 is a very prominent step-like decrease in the mass distribution at a voltage of about 8 mV. This step-like decrease occurs both north and south of the ring plane (compare Figures 8 and 9), but is not present on the outbound pass where the slope is more nearly independent of z. Apparently, this is a local feature not present at all points around the ring.

In addition to the distribution of voltage amplitudes, F(V), it is also of interest to compute the root-mean-squared (r.m.s.) voltage, V_{rms}, which will be used in the next section to compute the r.m.s. mass of the dust particles. For purposes of computing V_{rms}, it is useful to plot $V^2F(V)$, so that we can judge whether there is enough dynamic range available to give an accurate determination of the r.m.s. voltage. Figure 10 shows a plot of $V^2F(V)$ near the center of the first ring plane crossing (–70 km < z < 70 km). The r.m.s. voltage squared V_{rms}^2, is given by the area under the curve. It is evident that the area under the curve is reasonably well determined, since there does not appear to be a large contribution from impacts that are either above or below the available dynamic range (i.e., less than about 1.6 mV, or greater than about 65 mV). The r.m.s. voltage near the ring plane, from –70 km < z < 70 km, computed by integrating under the curve is V_{rms} = 6.65 mV.

Since the voltage measured by the dipole antenna depends somewhat on the location of the impact, the best way to characterize the absolute voltage spectrum of the dust impacts is by measuring the voltage on the monopole antenna. Since the monopole gives the voltage between the antenna and the spacecraft body, this voltage is expected to be independent of the location of the impact. Figure 11 shows the voltage spectral density on the monopole as obtained from the low-rate spectrum analyzer near the center of the ring plane crossing (–70 km < z < 70 km). The voltage spectral density has been plotted on a log-log plot so that a power-law distribution appears as a straight line. For low frequencies (below about 4000 Hz), the spectral density is proportional approximately to ,$(1/f)^2$ and as predicted by the theory of Aubier *et al.* [1983] at high frequencies (above about 4000 Hz), the spectral density is proportional approximately to $(1/f)^4$.

Root-Mean Square Mass

Figure 12 illustrates what happens when a small high-velocity particle traveling at a speed of many kilometers per second strikes the surface of the spacecraft. Upon impact the kinetic energy of the particle is converted into heat which vaporizes both the particle and part of the target material, thereby producing a small partially ionized cloud of gas. Some of the electrons (-Q) in this rapidly expanding plasma cloud escape leaving the spacecraft body with a charge Q. Laboratory measurements show that the charge released is proportional to the mass of the impacting particle, i.e., Q = km, where k is a constant that depends on the speed of the particle. The mass-to-charge conversion constant k has been measured for various materials and impact velocities in the laboratory by Grün [1981], and is approximately k = 0.4 C g^{-1} for dielectric particles (such as water ice) striking a metal target at a speed of 16 km s^{-1}, which is typical of the impact velocities that occur at the Cassini ring plane crossings. It should be noted that laboratory measurements are not available for the exact target material (conducting paint) that is actually present on the high gain antenna, so the above value for the charge-to-mass conversion constant is at best an intelligent guess, and could very well be in error by a substantial factor. After the impact, the escaping electrons cause a nearly radial electric field to develop in the plasma cloud between the spacecraft body and the escaping electrons. Our current view is that it is this polarization electric field that induces the voltages in the electric antennas. On Cassini the antenna voltage can be measured by the RPWS in two ways: via waveform measurements using the x-axis dipole antenna, and via spectrum measurements using the w-axis monopole antenna.

Since the voltage induced on the dipole antenna involves a differential measurement, which is inherently sensitive to the impact location, the best way to estimate the mass of the impacting particle is by measuring the voltage on the monopole antenna, which is directly related to the charge Q remaining on the spacecraft body.

As the plasma cloud expands over the monopole antenna, the high frequency receiver detects a voltage pulse, Q/C, that is related to the effective capacity C of the spacecraft body. The capacity of the spacecraft body is estimated to be about C = 200 pF [Gurnett *et al.*, 2004]. As a simple model, the voltage on the monopole antenna can be represented by the following waveform [Aubier *et al.*, 1983]

$$V(t) = 0 \qquad t \le 0 \quad \text{and}$$

$$V(t) = \left(1 - e^{-t/\tau}\right)(Q/C)\beta \qquad t > 0 \quad , \tag{3}$$

where τ is the rise time of the impact ionization process and $\beta \approx 0.4$ is a factor that takes into account the voltage reduction due to the known base capacity of the antenna, i.e. $\beta = C_A/(C_A + C_B)$, where C_A is the antenna capacity and C_B is the base capacity (see Figure 12). It is easy to show that the Fourier transform of V(t) is

$$V(\omega) = \frac{Q}{C}\left(-\frac{1}{i\omega} + \frac{1}{i\omega - 1/\tau}\right)\beta . \tag{4}$$

The voltage spectrum is then given by

$$V^2 = \left|V(\omega)\right|^2 = \frac{Q^2\beta^2}{C^2\omega^2}\left(1 - \frac{1}{1 + 1/\tau^2\omega^2}\right) . \tag{5}$$

For low frequencies, $\tau^2\omega^2$ << 1, the term $1/(1+1/\tau^2\omega^2)$ is much less than 1 and can be neglected compared to 1. Thus, at low frequencies the spectral density is proportional to $(1/f)^2$, i.e.

$$V^2 = \frac{Q^2\beta^2}{C^2\omega^2} = \frac{Q^2\beta^2}{(2\pi)^2 C^2 f^2}. \tag{6}$$

For high frequencies, $\tau^2\omega^2$ >> 1, the spectral density function simplifies to

$$V^2 = \frac{Q^2\beta^2}{C^2\tau^2\omega^4} = \frac{Q^2\beta^2}{(2\pi)^4 C^2\tau^2 f^4}, \tag{7}$$

and the spectral density is then proportional to $(1/f)^4$. As shown in Figure 11 the voltage spectral density on the monopole antenna has a very good fit to this expected $(1/f)^4$ frequency dependence. Taking $\tau^2\omega_c^2 = 1$ as defining the critical frequency that distinguishes the low frequency region from the high frequency region, we can obtain the rise time τ. From Figure 11 one can see that the critical frequency, $f_c = (1/2\pi)\omega_c$, is approximately 4000 Hz. The corresponding rise time is then $\tau = 40$ μs.

Since the charge Q released by the impact is directly proportional to the mass of the impacting particle, after substituting $Q = km$ into equation (7) it is easy to see that the voltage spectrum caused by one dust impact is given by

$$V^2 = \frac{k^2 m^2 \beta^2}{(2\pi)^4 C^2\tau^2 f^4}. \tag{8}$$

Next we show that by measuring the voltage spectrum of many impacts, we can obtain the r.m.s. mass distribution of the dust particles. Integrating from the minimum mass to the maximum mass of the detected dust particles, we can compute the r.m.s. mass, which is given by

$$m_{rms} = \sqrt{\langle m^2 \rangle} = \sqrt{\frac{1}{N}\int_{m_{min}}^{m_{max}} \frac{dN}{dm} m^2 dm}\ . \tag{9}$$

where N is the total number of particles. Similarly, we can compute the r.m.s. voltage, which is given by

$$V_{rms} = \sqrt{\langle V^2 \rangle} = \sqrt{\frac{1}{N}\int_{m_{min}}^{m_{max}} \frac{dN}{dm} V^2 dm}\ . \tag{10}$$

Comparing these two equations with equation (8) we see that the relationship between the r.m.s. voltage and the r.m.s. mass is given by

$$V_{rms}^2 = \frac{k^2 m_{rms}^2 \beta^2}{(2\pi)^4 C^2 \tau^2 f^4} \quad . \tag{11}$$

Since the voltage spectral density is the average voltage spectrum produced by one impact, we must multiply the above equation by the impact rate, R, to obtain the voltage spectral density produced by many impacts. The voltage spectral density produced by an impact rate R is then given by

$$\frac{V_{rms}^2}{\Delta f} = \frac{R k^2 m_{rms}^2 \beta^2}{(2\pi)^4 C^2 \tau^2 f^4} = A\left(\frac{1}{f}\right)^4 , \tag{12}$$

where A is a coefficient that can be computed from the measured voltage spectral density. The parameters that we have adopted for computing the r.m.s. mass are as follows: C = 200 pF, τ = 40 μs, k = 0.4 C g^{-1} and $\beta \approx 0.4$. The average impact rate for the spectrum in Figure 11 is R = 974/s. Substituting these parameters into equation (12) and canceling the common $(1/f)^4$ terms then gives the following relationship between the coefficient A and the r.m.s. mass

$$A = 2.5 \times 10^{26} m_{rms}^2 \text{ Volts}^2 \text{ Hz}^2 . \quad (13)$$

The coefficient A can be obtained by fitting a straight line to the f^{-4} spectrum in Figure 11. This spectrum can be described by the following equation,

$$\log\left(\frac{V^2}{\Delta f}\right) = \log\left(Af^{-4}\right) = -4\log f + \log\left(A\right) \quad . \quad (14)$$

By evaluating one point from this line, we obtain

$$A = 1.5 \times 10^6 \text{ Volts}^2 \text{ Hz}^2 . \quad (15)$$

Substituting this value of A into equation (13) then gives

$$m_{rms} = 7.7 \times 10^{-11} g . \quad (16)$$

This result shows that the r.m.s. mass of dust particles near the ring plane is on the order of a few times 10^{-11} g, a result that is similar to previous work by Aubier *et al.*, [1983] for the Voyager 2 ring plane crossing. Assuming that the dust particles are made of water ice, which has a density of 0.92 g cm^{-3}, the corresponding r.m.s. particle radius is 2.6 μm.

We can now return to the calibration of the mass scales shown on the bottoms of Figure 7, 8 and 9. Since these spectrums were all obtained from the E_x dipole antenna, we cannot use the same mass to voltage conversion constant that was used for the monopole antenna. To provide a mass calibration for these spectrums we assume that the r.m.s. voltage on the dipole antenna corresponds to the same r.m.s. mass that was detected by the monopole antenna. From the $V^2F(V)$ spectrum shown in Figure 10 it is easy to calculate the r.m.s. voltage on the dipole antenna, which is V_{rms} = 6.65 mV. The mass to voltage conversion constant for the dipole antenna is then $\kappa = 6.65$ mV/7.7 $\times 10^{-11}$g = 8.64×10^{10}mVg^{-1}. This conversion constant has been used to determine the mass scales at the bottoms of Figures 7, 8 and 9. The particle size scale, indicated by the arrows labeled 1 μm, 2 μm, and 3 μm, has been computed assuming that the particles are spheres with the density of water ice, $\rho = 0.92$ g cm^{-3}.

CHAPTER V

CALCULATION OF OPTICAL SCATTERING PROPERTIES

At present the Cassini imaging system has not detected any scattered light from the region of the rings (2.634 and 2.630 R_S) where these observations were obtained [J. Burns, personal communication]. Since it may be possible later in the Cassini mission to select optical viewing geometries that are more favorable for detecting scattered light from this region of the rings, to facilitate possible future comparisons with optical measurement in this chapter we calculate the optical depth and the angular distribution of the scattered light using the dust parameters presented in the previous section.

Calculation of the Optical Depth

A crucial parameter in any calculation of light scattering by small particles is the optical depth. The optical depth, τ, which gives a measure of the opacity of a medium is defined by the equation

$$F(l) = F_0 e^{-\tau} \quad , \tag{17}$$

where F_0 is the incident flux, F(l) is the flux reaching the observation site at a distance l in the medium. The calculation of optical depth is based on a famous problem, first considered by Mie in 1908, and now widely referred to as Mie theory. For a discussion of the history of Mie theory see Bohren and Huffman [1983]. The differential optical depth given by Bohren and Huffman [1983] due to particles of size from a to a + da is given by as the following equation

$$d\tau = Q_{ext}(x)\pi a^2 n(a) l da \quad , \tag{18}$$

where $Q_{ext}(x)$ is the extinction efficiency (the ratio of the extinction cross section to the geometrical cross section), πa^2 is the geometrical cross section of the particle, l is the effective path length through absorbing medium, and n(a) is the differential spectrum of particle size.

The differential spectrum of particle size is defined such that

$$\int n(a) da = n \quad , \tag{19}$$

where n is the number density given by equation (2). In equation (18) the quantity x is defined as the normalized quantity, $x=2\pi a/\lambda$, where λ is the wavelength of the light.

To carry out the computation of the optical depth, it is useful to first compute the extinction efficiency for a single dust particle. According to the Mie theory, which provides a complete mathematical-physical theory of the scattering of electromagnetic radiation by spherical particle, the extinction efficiency $Q_{ext}(x)$ for a dust particle is given by

$$Q_{ext} = \frac{2\pi}{k^2 \pi a^2} \sum_{n=1}^{\infty} (2n+1)(|a_n|^2 + |b_n|^2) \quad , \tag{20}$$

where, a_n and b_n, are the scattering coefficients for the electromagnetic normal modes and are given by [see Bohren and Huffman, 1983]

$$a_n = \frac{m\psi_n(mx)\psi_n'(x) - \psi_n(x)\psi_n'(mx)}{m\psi_n(mx)\xi_n'(x) - \xi_n(x)\psi_n'(mx)} \quad ,$$

and

$$b_n = \frac{\psi_n(mx)\psi_n^{'}(x) - m\psi_n(x)\psi_n^{'}(mx)}{\psi_n(mx)\xi_n^{'}(x) - m\xi_n(x)\psi_n^{'}(mx)} \ .$$

The function $\psi_n(x)$ and $\xi_n(x)$ are Riccati-Bessel functions and are defined as

$$\psi_n(x) = xj_n(x) \ ,$$

$$\xi_n(x) = xh_n^{(1)}(x) \ ,$$

Where $j_n(x)$ is the spherical Bessel function and $h_n^{(1)}(x)$ is the Hankel function of the first kind [Jackson,1962]. The quantity m is the complex refractive index of the particle, the real part of which is the ratio of the speed of light divided by the phase velocity, and the imaginary part of which is proportional to the absorptivity. Since the particles in Saturn's rings are believed to be water ice, which has a very low absorptivity, we shall assume that m is purely real and is given by the index of refraction of water ice (i. e., m = 1.33).

Appendix B gives the values of $Q_{ext}(x)$ computed using Mathematica. The first line at the top of the table shows the cutoff value, n_{max}, of the summation used in calculating $Q_{ext}(x)$ and the first column on the left list the values of x used in the computation. Note that the n_{max} value required to obtain a constant asymptotic value for $Q_{ext}(x)$ is strongly dependent on the value of x. The larger the value of x is the larger the value of n required for convergence to a nearly constant value of $Q_{ext}(x)$. We can see, from this table, that $Q_{ext}(x)$ changes very little after n=30 even for very large x values, so we can neglect all the terms after n=30. So to calculate $Q_{ext}(x)$ we ran the Mathematica program from n=0 to n=30. In order to make sure our program worked properly, we tested it by generating a plot (Figure 13) and comparing it to a comparable plot given by [L. Spitzer, 1968]. Then we set a specific wavelength, λ = 500nm and generated the plot shown in Figure 14. this plot shows how the extinction efficiency changes as a function of particle size. The Mathematica code used in this computation is given in Appendix C.

Next, we derive n(a), the differential distribution of particle size, since we want to calculate the optical depth due to a range of particle sizes. Since the differential size distribution is determined by the amplitude distribution of peak voltages, we must relate n(a) to F(V), see Figure 15. Using the chain rule, n(a) can be written as

$$n(a) = \frac{dn}{da} = \frac{dn}{dV}\frac{dV}{da} = n_0 F(V)\frac{dV}{da}, \tag{21}$$

where we have used dn/dV = n_0 F(V). For the detailed computation it is useful to have an analytic representation for F(V). To obtain analytical representation we have shown that the following power law provides a very good fit to the amplitude distribution of peak voltages given in Figure 15,

$$F(V) = A_1 V^{-2.4} \ , \tag{22}$$

where A_1 = 1.55 $(mV)^{1.4}$. This power law implies that the mass spectrum varies as $m^{-2.4}$. Since the peak voltage of dust impacts measured by dipole antenna can be express as,

$$V = \kappa m = \kappa \frac{4}{3}\pi\rho a^3 \ , \tag{23}$$

where, as discussed in the previous section, κ = 8.64 $\times 10^{10}$mVg^{-1} is mass to voltage conversion constant for the dipole antenna and ρ = 0.92 g cm^{-3} is the density of the particle, which as mentioned earlier is assumed to be water ice. Doing the necessary computations gives

$$\frac{dV}{da} = 4\kappa\rho\pi a^2 , \tag{24}$$

and after substitute equations (22), (23) and (24) into equation (21), we get

$$n(a) = n_0 F(a) = A_2 a^{-5.2}, \qquad (25)$$

where n_0 is taken to be the number density at the ring plane crossing, which from the previous section is approximately $n_0 = 6 \times 10^{-9}$ cm^{-3}, and the constant A_2 in the second term (using the nominal parameters, $\kappa = 8.64 \times 10^{10}$mVg^{-1} , and $\rho = 0.92$ g cm^{-3})

is $A_2 = 3 n_0 A_1 (\frac{4\kappa\pi\rho}{3})^{-1.4} = 2.066 \times 10^{-24}cm^{1.2}$.

Since the extinction efficiency is a function of x it is convenient to compute the total optical depth by changing the variable in n(a) from a to x. By doing that, the optical depth is given by

$$\tau = \int_{x_{\min}}^{x_{\max}} Q_{ext}(x) A_2 \pi l (4\pi)^{2.2} x^{-3.2} dx, \qquad (26)$$

where we have used a wavelength of $\lambda = 500$nm (roughly in the middle of the visible light range) for computing the upper and lower limits of the integral. The upper and lower limits of the integral are determined from the voltage range (1.6mv to 65mv) of the pulses that can be detected by RPWS. To simplify the calculation, we use the nominal density at the ring plane, $n_0 = 6 \times 10^{-9}$ cm^{-3}, times an effective north-south path length, $l_{eff} = 417$ km, for the thickness of the ring plane. The effective path length was computed by requiring that $n_0\, l_{eff} = \int n\, dz$, where n has been computed from equation (2) using the best fit Gaussian representation of the impact rate discussed in the previous section. Using the integral from x_{min} to x_{max} in equation (26), which corresponds to a particle size of $a = 1.7$ µm, these parameters give an optical depth of $\tau = 4.26 \times 10^{-8}$. Since the power law spectrum undoubtedly extends well below the counting threshold, this optical depth only represents a lower limit to the true optical depth. To determine the possible effect of particles with sizes below the counting threshold, we have reduced the lower limit on the integral in equation (26) by a factor of ten, to a = 0.17 μm, while still keeping the same $m^{-2.4}$ power law spectrum. The result is that the optical depth increased by a factor of 14, to $\tau = 6.0 \times 10^{-7}$. At the present we do not know if either of these levels of optical scattering can be detected by the the Cassini imaging instrument. If we can eventually get a quantitative limit on the optical depth from the imaging instrument it may be possible to determine at what point the mass spectrum rolls over toward decreasing mass, as it must, since an $m^{-2.4}$ spectrum diverges at the low masses.

<u>Angular Distribution of Scattered Light</u>

Since the scattering of sunlight by the ring particles depends critically on the angle of the observations relative to incident sunlight, in order to aid in the planning of such observations by Cassini or any other future spacecraft mission to Saturn it is useful to compute the angular distribution of the scattered light. In this section we will compute a typical power pattern, $P(\theta)$ of the scattered sunlight based on our measurements of the number density and mass distribution of the detected ring particles.

As we discussed earlier, when a beam of light transverse a distance l through a homogeneous particulate medium, its intensity is exponentially attenuated from F_0 to $F(l)$ according to the equation

$$F(l) = F_0 e^{-\tau} \ . \tag{27}$$

The scattered light intensity along this path is then given by

$$\Delta F = F - F_0 = F_0(1 - e^{-\tau}) \ . \tag{28}$$

If the scattering medium is optically thin, τ « 1, the scattered light intensity is then given by

$$\Delta F = F_0 \tau \ . \tag{29}$$

It then follows that

$$d(\Delta F) = F_0 d\tau \ , \tag{30}$$

gives the incremental scattered flux due to particles in the size range a to a +da, which produce an incremental optical depth dτ.

The amount scattered due to particle of size a can also be expressed as,

$$d(\Delta F) = \int P(\theta, a) d\Omega da \ , \tag{31}$$

where P(*θ*, *a*) is the incremental power pattern and *θ* is the angle to the observer relative to the incident light beam. The above equation can also be written as

$$P(\theta, a) = A(a) B(\theta, a) \tag{32}$$

A(*a*) is a function of the particle size only, and *B*(*θ*, *a*) is the normalized power pattern. Equation (32) is a plausible assumption made in this thesis. The form of the power pattern is obtained by comparisons to the exact power pattern calculated by Bohren and Huffman (1983), and is shown in Figure 4.9 of their book. Although we could do the calculation from first principles, it turns out that for substantial range of scattering angles the power pattern is well represented by a Gaussian function of the form

$$B(\theta, a) = e^{-\sin^2\theta/\sigma^2(a)} \ , \tag{33}$$

where

$$\sigma(a) = \frac{b\lambda}{2a}\,. \tag{34}$$

The quality of fit is illustrated in Figure 16. The parameter b that gives the best fit is approximately 0.6. The above equations are for a fixed particle size. Since a broad range of particle sizes are present in the ring, to get the power pattern of the light scattered by these particles we must integrate over the entire particle size distribution. Integrating over the particle size and using equations (30) and (31), we get ,

$$\int da \int_0^\pi A(a)B(\theta,a)2\pi\sin\theta d\theta = \int F_0 d\tau da\,, \tag{35}$$

which simplifies to

$$\int_0^\pi A(a)B(\theta,a)2\pi\sin\theta d\theta = F_0 d\tau \;\;. \tag{36}$$

Noting that $A(a)$ is independent on θ this quantity can be factored out of the integral so that

$$A(a) = \frac{F_0 d\tau}{\int_0^\pi e^{-\sin^2\theta/\sigma^2(a)} 2\pi\sin\theta d\theta}\,. \tag{37}$$

This quantity will be useful later in the calculation of the power pattern.

Next, we must calculate dτ. As in the calculation of optical depth, our starting point is the formula for differential optical depth due to particle of size a, which is

$$d\tau = Q_{ext}(x)\pi a^2 n(a) l da \tag{38}$$

Since $x = 2\pi a / \lambda$ for a wavelength as 500nm it follows that $a = x / 4\pi\ \mu m$. Recall from equation (24) that

$$n(a) = A_2 a^{-5.2} . \tag{39}$$

Changing the variable from a to x , using $a = x/4\pi\ \mu m$, gives

$$d\tau = Q_{ext}(x) A_2 \pi l (4\pi)^{-2.2} x^{-3.2} dx . \tag{40}$$

From equation (36) we must next compute the quantity

$$A(x) = \frac{F_0 d\tau}{\int_0^{\pi} e^{-\sin^2\theta/\sigma^2(x)} 2\pi \sin\theta d\theta} \ . \tag{41}$$

Here,

$$\sigma(x) = \pi b / x = 1.88 / x . \tag{42}$$

Integrating the denominator of A(x), we get

$$\int_0^{\pi} e^{-\sin^2\theta/\sigma^2(x)} 2\pi \sin\theta d\theta = 2e^{-1/\sigma^2(x)} \sigma(x) \pi^{3/2} erf(1/\sigma(x)) , \tag{43}$$

where erf is the error function. The quantity, $P(\theta)$, is then given by

$$P(\theta) = \int_{x_{\min}}^{x_{\max}} \frac{F_0 d\tau}{2e^{-1/\sigma^2(x)} \sigma(x) \pi^{3/2} eri(1/\sigma(x))} e^{-\sin^2\theta/\sigma^2(x)} dx \ , \tag{44}$$

which, after substituting for τ(x) reduces to

$$P(\theta) = \int_{x_{\min}}^{x_{\max}} \frac{Q_{ext}(x) A_2 \pi l (4\pi)^{2.2} x^{-3.2}}{2e^{-1/\sigma^2(x)} \sigma(x) \pi^{3/2} efr(1/\sigma(x))} e^{-\sin^2\theta/\sigma^2(x)} dx \ , \tag{45}$$

or

$$P(\theta) = K \int_{x_{\min}}^{x_{\max}} \frac{Q(x) x^{-3.2}}{e^{-1/\sigma^2(x)} \sigma(x) erf(1/\sigma(x))} e^{-\sin^2\theta/\sigma^2(x)} dx \ . \tag{46}$$

where K is a constant which doesn’t change the relative power pattern. Figure 17 shows a plot of the normalized power pattern, $P(\theta) / P(0)$, as a function of θ , for two cases. The curve marked a_{min} = 1.7 μm corresponds to the integration from x_{min} to x_{max} given in the above equation, i.e., from the detection threshold, 1.6 mV, which corresponds to a size of a = 1.7 µm, to the maximum voltage that can be detected, 65 mV, which corresponds to a particle size of a = 5.8 µm. As can be seen, the power pattern is sharply peaked in the forward direction, with a full width at half maximum (FWHM) of 9°. The very narrow width is expected, since most of the particles are much larger than the wavelength of the incident light, which produces a very narrow diffraction pattern. Since we expect that there are many smaller particles below the 1.7µm detection threshold, we have decreased the lower limit of integration by a factor of ten, just as we did for the calculation of the optical depth. The resulting curve, marked a_{min} = 0.17 µm in Figure 17, has a much broader power pattern, with a FWHM of 21°. The broader power pattern is to be expected, since smaller particles produce a broader diffraction pattern. From this illustration we can see that with more small particles, the power pattern is more isotropic.

CHAPTER VI

DISCUSSION AND CONCLUSIONS

In this paper we have described and analyzed the dust impacts detected by the Cassini RPWS during the first pass through Saturn's ring plane. Although the Cassini and Voyager 2 ring plane crossings occurred in different parts of the ring system and the instrumental parameters are somewhat different, the peak number densities are quite similar. The number densities at the two Cassini ring plane crossings at 2.634 and 2.630 R_S, are slightly smaller, 5.6×10^{-3} and 6.3×10^{-3} m^{-3}, but still very similar to the number density (15×10^{-3} m^{-3}) given by Tsintikidis *et al.* [1994] for the Voyager 2 ring plane crossing. Also the north-south impact rate profiles for both the Cassini and Voyager 2 ring plane crossings fit the sum of two Gaussians, thereby indicating the presence of "core" and "halo" components. The fit parameters are, however, somewhat different. For the Cassini crossings the north-south thickness, $2L_1$, of the "core" component was about 300 km, compared to 962 km for the "core" component during the Voyager 2 ring plane crossing [Tsintikidis *et al.*, 1994] and the north-south thickness of the "halo" component was about 700 km, compared to 3376 km for the "halo" component during the Voyager 2 ring plane crossing.

Because of the improved dynamic range and the availability of simultaneous measurements from both dipole and monopole antennas, the Cassini RPWS instrument has a much better capability than the Voyager plasma wave instrument for determining the mass distribution of the impacting particles. Using the impact coupling model developed by Aubier *et al.* [1983], we developed a formula that describes the relationship between r.m.s. voltage detected by the monopole antenna and the r.m.s. mass. Using this relationship, the r.m.s. mass of the dust particles near the inbound ring plane crossing was estimated to be 7.7×10^{-11}g. A similar value was obtained for the outbound ring plane crossing. Assuming that the dust particles are water ice with a mass density of 0.92g/cm^3, the corresponding r.m.s. radius is 2.6 µm. This estimate of the size of the particle depends critically on the assumed mass-to-charge conversion constant, which from the best available data was assumed to be k = 0.4 C g^{-1}. Because of the current lack of laboratory data for the likely target material on the high gain antenna, this value could very well be in error by a substantial factor. However, we note that the particle radius only depends on the cube root of the mass-to-charge conversion constant, so even an error factor of ten would only change the estimated radius of the particles by a little more than a factor of two. So it is clear that the typical radius of impacting particles is on the order of a few microns. From the distribution of voltage amplitudes we also showed that the mass distribution of the impacting particles detected near the ring plane decreased with increasing mass, varying approximately as m^{-2} near the ring plane. As the distance from the ring plane increased the slope of the mass distribution tends to increase, varying approximately as m^{-4} at a distance of 500 km from the ring plane during the inbound ring plane crossing. This north-south dependence suggests that the larger particles do not extend as far from the ring plane. Also, well away from the ring plane the particle mass distribution on the inbound crossing showed a notable step-like decrease for particle radii greater than about 2 to 3 µm. This step-like decrease suggests that some local process may be acting to erode or modify the distribution of larger particles that are orbiting at inclined angles to the ring plane.

Using the measured data parameters, we have calculated the optical depth of the dust particles detected by RPWS and the angular distribution of the scattered light. For the minimum particle size that can be detected by the RPWS, which is about a_{min} = 1.7 μm, and a wavelength of 500 nm, the computed optical depth normal to the ring plane is about $\tau = 4.26 \times 10^{-8}$. If the mass spectrum continues with the same $m^{-2.4}$ power law down to significantly smaller particle sizes than can be detected by the RPWS, which seems highly likely, then the optical depth increases substantially. For example, if the particle mass spectrum were to continue with the same power law dependences down to a_{min} = 0.17 μm, the optical depth would increase to $\tau = 6.0 \times 10^{-7}$. To compare with actual optical measurements by Cassini, these optical depths must be multiplied by the secant of the viewing angle relative to the normal to the ring plane. Because of the secant dependence it is obviously favorable to make this viewing angle as large as possible in order to increase the optical depth. However, the angle must not be made so large and the viewing geometry must not be such that the path length integration extends over the region of the ring where no dust impact measurements were made. For this purpose it is desirable to view the rings along a direction approximately tangent to the direction of motion of the ring plane particles.

A crucial parameter for planning any future ring plane imaging observations is the viewing angle relative to the sun. Using a minimum particle size of a_{min} = 1.7 μm and a wavelength of 500 nm, our calculations show that the power pattern of the scattered light is sharply peaked in the forward direction with a FMHM is about 9°. These results are within our expectation since the particle sizes are much larger than the assumed wavelength diffraction causes the radiation to be strongly directed into the forward direction. Since the Cassini imaging system cannot make observations within about 15° from the sun because of potential damage to the camera, the rapid decrease in the scattered light intensity with increasing angle from the sun represents a serious problem for detecting these particles. If the size distribution of dust particles extends to a lower level by a factor of 10 with the same $m^{-2.4}$ power law distribution, the FWHM increases to 21°, which improves the observational situation considerably. Since our conversations with the Cassini imaging team suggest that the minimum detectable optical depth is about 10^{-6}, it is obviously going to be difficult to detect these particles by optical means, although it may be possible if the observations are carefully planned.

REFERENCES

Aubier, M.G., Meyer-Vernet, N., Pedersen, B.M., 1983. Shot noise from grain and particle impacts in Saturn's ring plane. *Geophys. Res. Lett., 10,* 5-8.

Bohren, C.F., and Huffman, D.R., 1983. Absorption and scattering of light by small particles, Wiley-Interscience, New York.

Esposito, L.W., Cuzzi, J.N., Holberg, J.B., Marouf, E.A., Tyler, G.L., Porco, C.C., 1984. Saturn's rings: Structure, dynamics, and particle properties. In: Gehrels, T. and Matthews, M.S. (Eds.), *Saturn*, University of Arizona Press, Tucson, pp. 463-545.

Grün, E., 1981. Experimental studies of impact ionization. *Eur. Space Agency Spec. Publ., ESA SP-155,* pp. 81-90.

Gurnett, D. A., Scarf, F. L., Fredricks, R. W., and Smith, E. J., 1978. The ISEE 1 and 2 plasma wave investigation. *IEEE Trans. Geosci. Electron., GE-16*, 225.

Gurnett, D.A., Grün, E., Gallagher, D., Kurth, W.S., Scarf, F.L., 1983. Micron-sized particles detected near Saturn by the Voyager plasma wave instrument. *Icarus, 53*, 236-254.

Gurnett, D. A., Kurth, W. S., Shaw, R. R., Roux, A., Gendrin, R., Kennel, C. F., Scarf, F. L., and Shawhan, S. D., 1992. The Galileo plasma wave investigation. *Space Sci. Rev., 60*, 341.

Gurnett, D. A., Persoon, A. M., Randall, R. F., Odem, D. L., Remington, S. L., Averkamp, T. F., DeBower, M. M., Hospodarsky, G. B., Huff, R. L., Kirchner, D. L., Mitchell, M. A., Pham, B. T., Phillips, J. R., Schintler, W. J., Sheyko, P., and Tomash, D. R., 1995. The polar plasma wave instrument. *Space Sci. Rev., 71*, 597.

Gurnett, D.A., Kurth, W.S., Kirchner, D.L., Hospodarsky, G.B., Averkamp, T.F., Zarka, P., Lecacheux, A., Manning, R., Roux, A., Canu, P., Cornilleau-Wehrlin, N., Galopeau, P., Meyer, A., Bostrom, R., Gustafsson, G., Wahlund, J.-E., Aahlen, L., Rucker, H.O., Ladreiter, H.-P., Macher, W., Woolliscroft, L.J.C., Alleyne, H., Kaiser, M.L., Desch, M.D., Farrell, W.M., Harvey, C.C., Louarn, P., Kellogg, P. J., Goetz, K. Pedersen, A., 2004. The Cassini radio and plasma wave science investigation. *Space Sci. Rev., 114*, 395-463.

Jackson, W. D., 1962. *Classical Electrodynamics*, Wiley, New York. pp. 540.

Kempf, S., Srama, R., Horányi, M., Burton, M., Helfert, S., Moragas-Klostermeyer, G., Roy, M., Grün, E., 2005a. High-velocity streams of dust originating from Saturn. *Nature, 433*, 289-291.

Kempf, S., Srama, R., Postberg, F., Burton, M., Green, S.F., Helfert, S., Hillier, J.K., McBride, N., McDonnell, J.A.M., Georg, M.K., Moragas-Klostermeyer, G., Roy, M., Grün, E., 2005b. Composition of Saturnian stream particles. *Science, 307*, 1274-1276.

Kurth, W.S., T.F. Averkamp, D.A. Gurnett, and Z. Wang, 2006. Cassini RPWS observations of dust in Saturn's E ring, *Planet. Space Sci.*, in press.

Spitzer, L., 1968. Diffuse matter in space. *Interscience Tracts On Physics and Astronomy*. Fig. 3.1

Matson, D.L., Spilker, L.J., Lebreton, J.-P., 2002. The Cassini/Huygens mission to the Saturnian system. *Space Sci. Rev., 104*, 1-58.

Meyer-Vernet, N., Aubier, M. G., and Pedersen, B. M., 1986. Voyager 2 at Uranus: Grain impacts in the ring plane. *Geophys. Res. Lett. 13*, 617.

Scarf, F.L., Gurnett, D.A., Kurth, W.S., Poynter, R.L., 1982. Voyager 2 plasma wave observations at Saturn. *Science, 215*, 587-594.

Smith, B.A., Soderblom, L., Beebe, R., Boyce, J., Briggs, G., Bunker, A., Collins, S.A., Hansen, C.J., Johnson, T.V., Mitchell, J.L., Terrile, R.J., Carr, M., Cook II, A.F., Cuzzi, J., Pollack, J.B., Danielson, G.E., Ingersoll, A., Davies, M.E., Hunt, G.E., Masursky, H., Shoemaker, E., Morrison, D., Owen, T., Sagan, C., Veverka, J., Strom, R., and Suomi, V.E., 1981. Encounter with Saturn: Voyager 1 imaging science results. *Science, 212*, 163-191.

Srama, R.; Ahrens, T. J.; Altobelli, N.; Auer, S.; Bradley, J. G.; Burton, M.; Dikarev, V. V.; Economou, T.; Fechtig, H.; Görlich, M.; Grande, M.; Graps, A.; Grün, E.; Havnes, O.; Helfert, S.; Horanyi, M.; Igenbergs, E.; Jessberger, E. K.; Johnson, T. V.; Kempf, S.; Krivov, A. V.; Krüger, H.; Mocker-Ahlreep, A.; Moragas-Klostermeyer, G.; Lamy, P.; Landgraf, M.; Linkert, D.; Linkert, G.; Lura, F.; McDonnell, J. A. M.; Möhlmann, D.; Morfill, G. E.; Müller, M.; Roy, M.; Schäfer, G.; Schlotzhauer, G.; Schwehm, G. H.; Spahn, F.; Stübig, M.; Svestka, J.; Tschernjawski, V.; Tuzzolino, A. J.; Wäsch, R.; Zook, H. A., 2004. The Cassini cosmic dust analyzer. *Space Sci. Rev., 114,* 465-518.

Tsintikidis, D., Gurnett, D.A., Granroth, L.J., Allendorf, S.C., Kurth, W.S., 1994. A revised analysis of micron-sized particles detected near Saturn by the Voyager 2 plasma wave instrument. *J. Geophys. Res., 99*, 2261-2270.

Warwick, J.W., Pearce, J.B., Evans, D.R., Romig, J.H., Alexander, J.K., Desch, M.D., Kaiser, M.L., Aubier, M., Leblanc, Y., Lecacheux, A., Pedersen, B.M., 1982. Planetary radio astronomy observations from Voyager 2 near Saturn. *Science, 215,* 582-587.

APPENDIX A

FIGURES

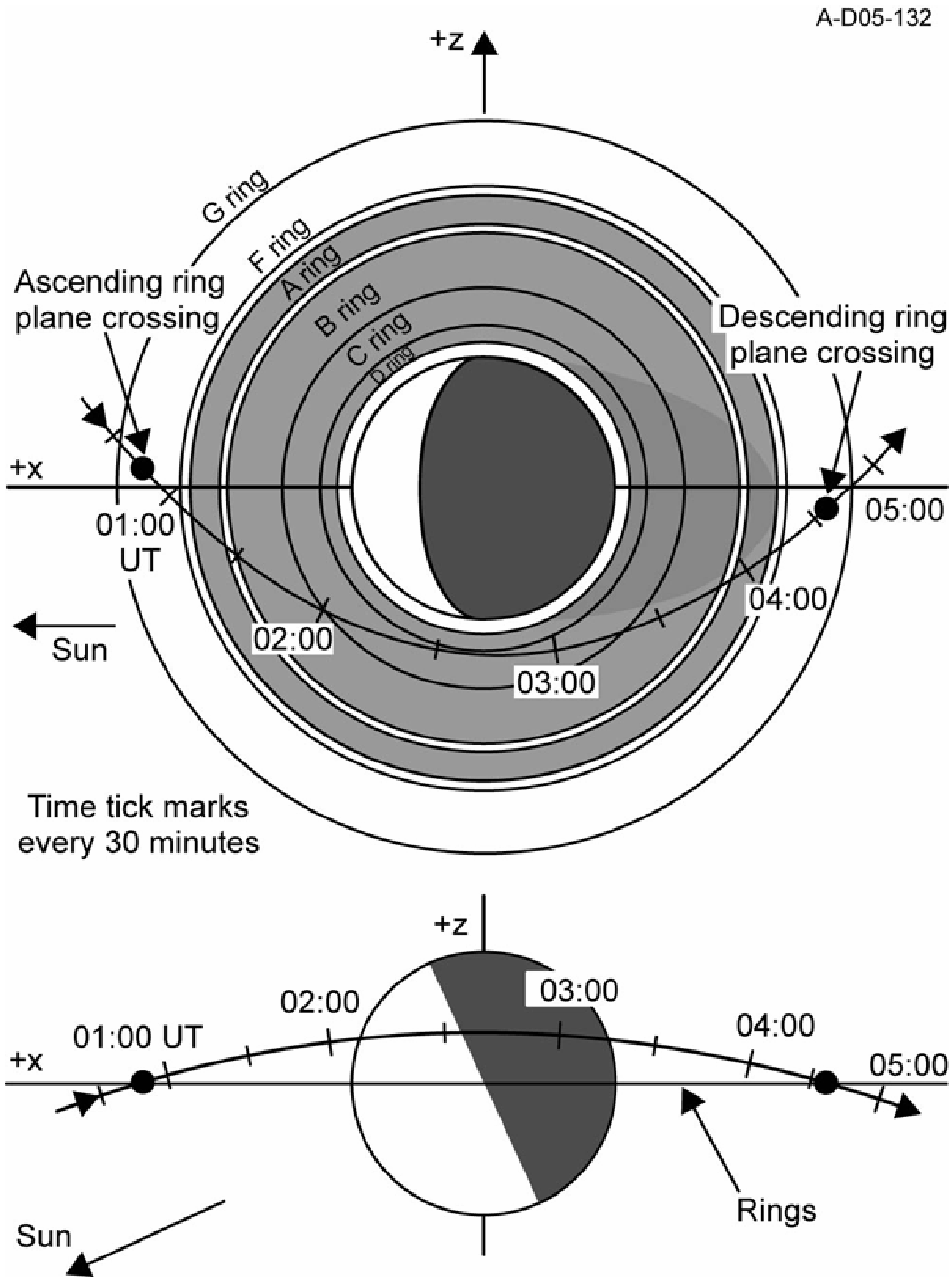

Figure A1. The trajectory of the Cassini spacecraft as it passed through the rings of Saturn on July 1, 2004.

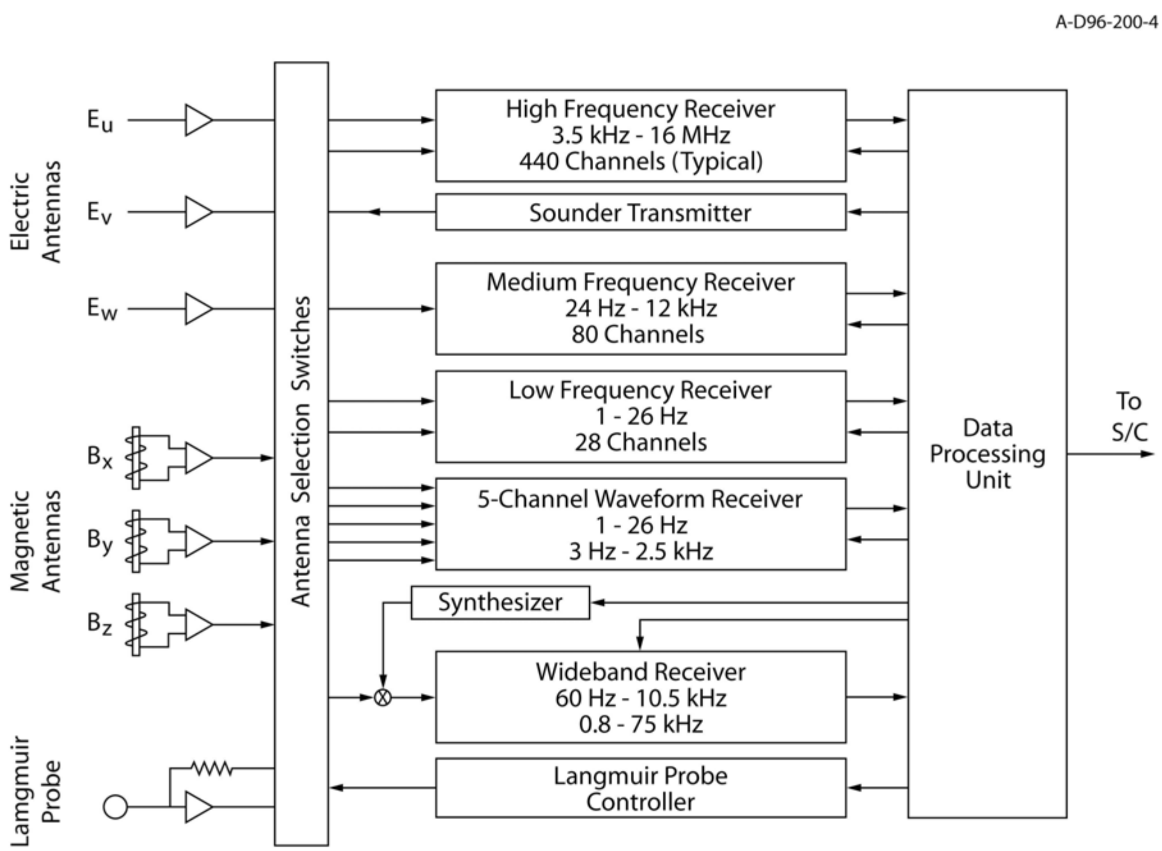

Figure A2. A functional block diagram of the RPWS instrument. The seven sensors, three electric, three magnetic, and the Langmuir probe are shown on the left side. In the middle, the several receivers which the instrument uses to analyze the signals are shown. The data management and control functions, as well as the interface with the spacecraft are shown as the data processing unit on the right side.

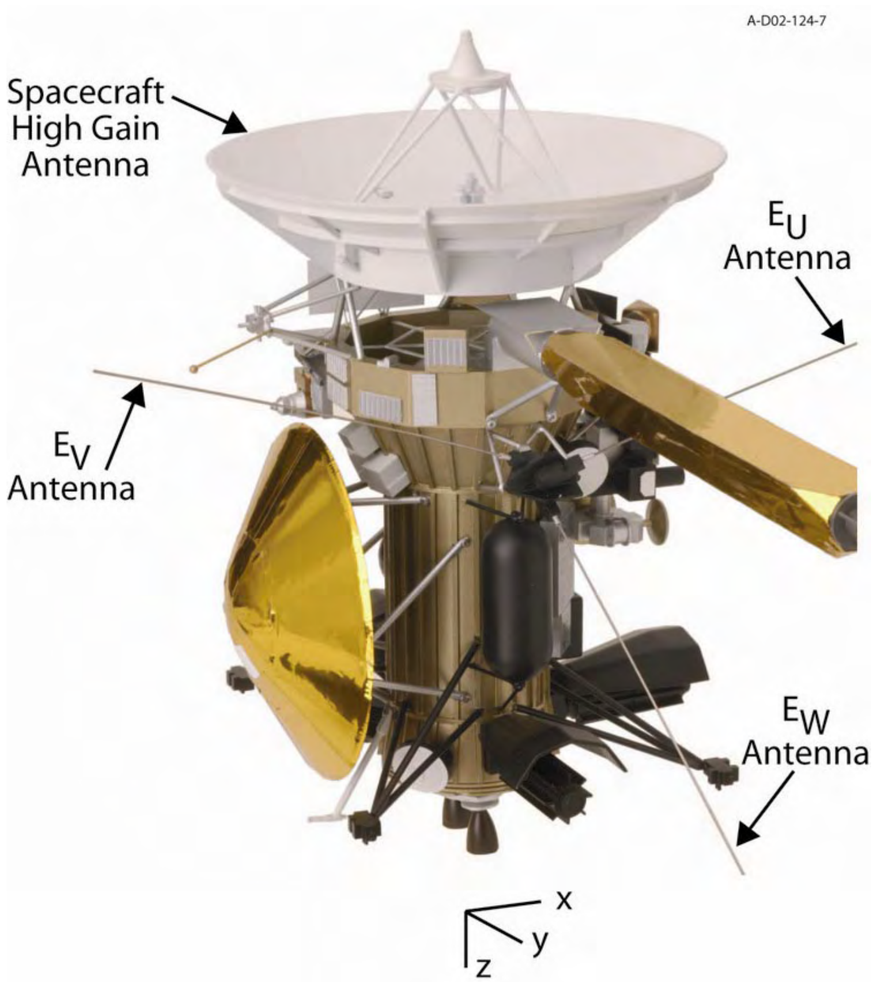

Figure A3. A sketch of the Cassini spacecraft showing the locations of the RPWS antennas and their relationship to other structures on the spacecraft. During the inbound and outbound ring plane crossing that occurred on July 1, 2004, the spacecraft orientation was such that most of the impacts occurred on the spacecraft high gain antenna.

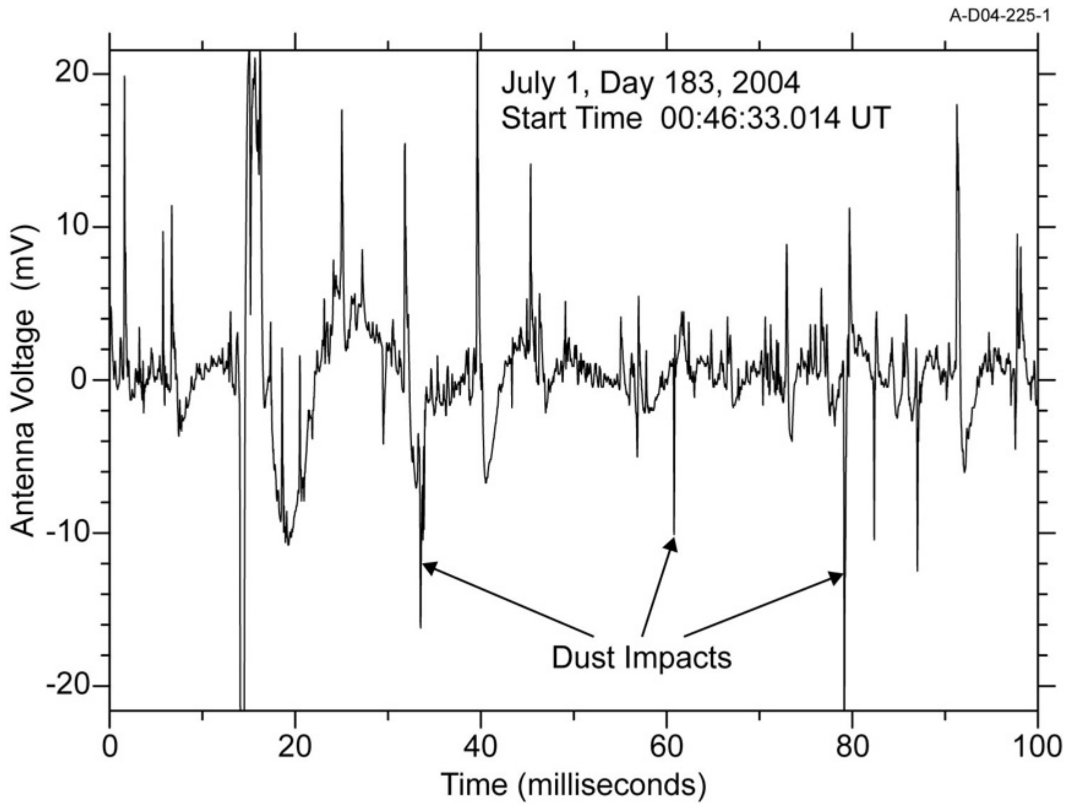

Figure A4. The wideband voltage waveform obtained from the $E_U - E_V$ electric dipole antenna during the first ring plane crossing. Some representative dust impact waveforms are shown by the arrows.

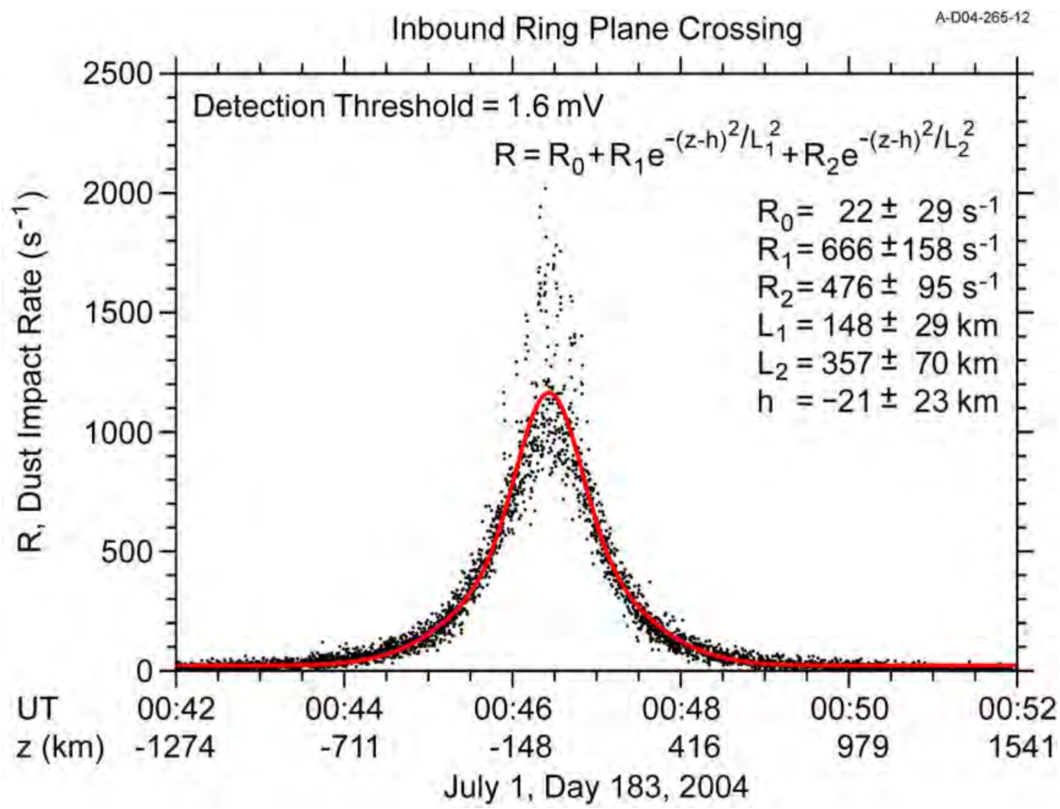

Figure A5. The impact rate R versus Universal Time (UT) and north-south distance z from the equatorial plane of Saturn for the inbound ring plane crossing. The best fit sum of two Gaussian curves is also shown by a red solid line.

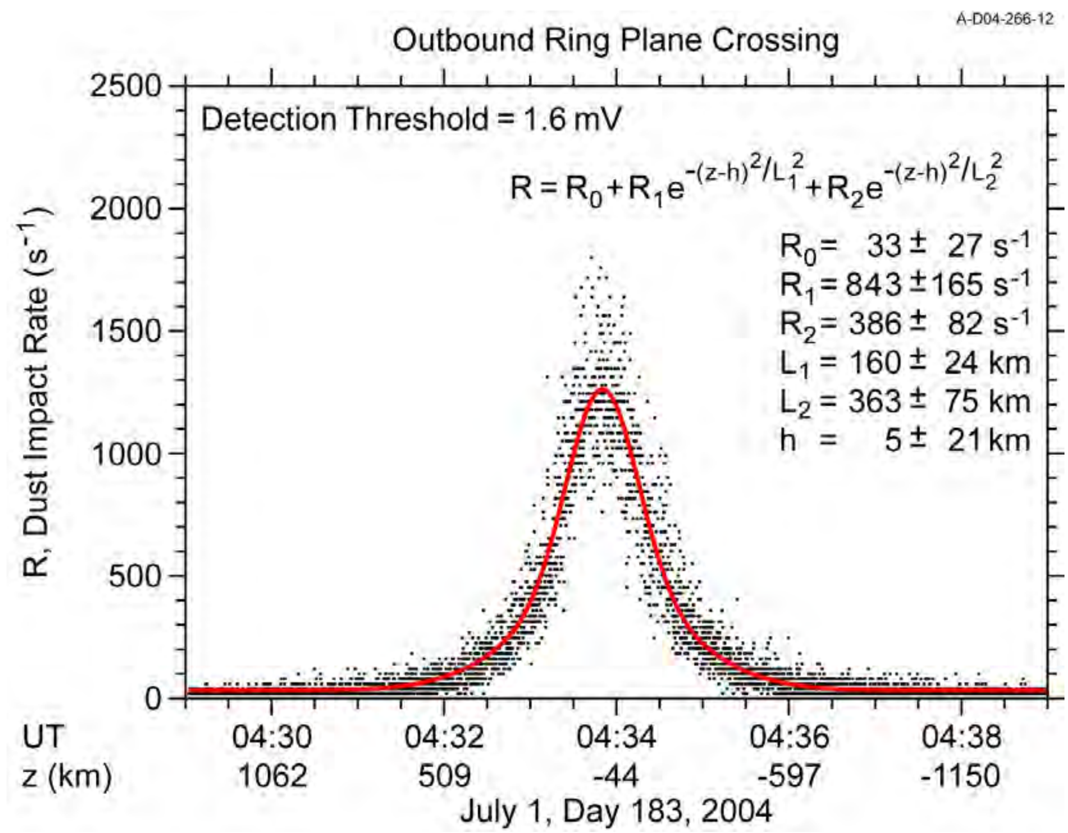

Figure A6. The impact rate R versus the time in UT and height z from the equatorial plane of Saturn for the outbound ring plane crossing. The best fit for a sum of two Gaussian curves is shown by the red solid line.

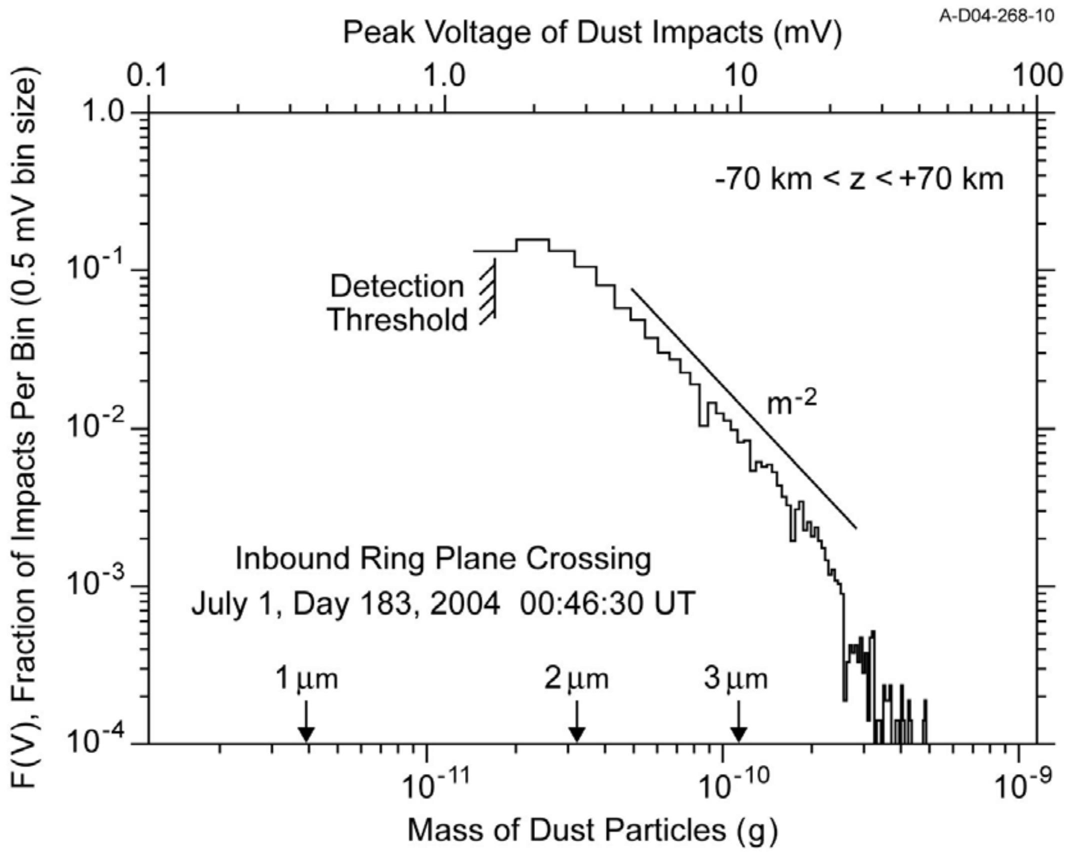

Figure A7. The amplitude distribution of the peak voltage of dust impacts observed near the center of the first ring plane crossing (−70 km < z < 70 km). The fraction of impacts per bin, F(V), is proportional to the differential mass distribution, dN/dm, and the peak voltage of dust impacts is proportional to the mass of the dust particles. Above about 1 mV, the differential mass distribution dN/dm varies approximately as m^{-2}.

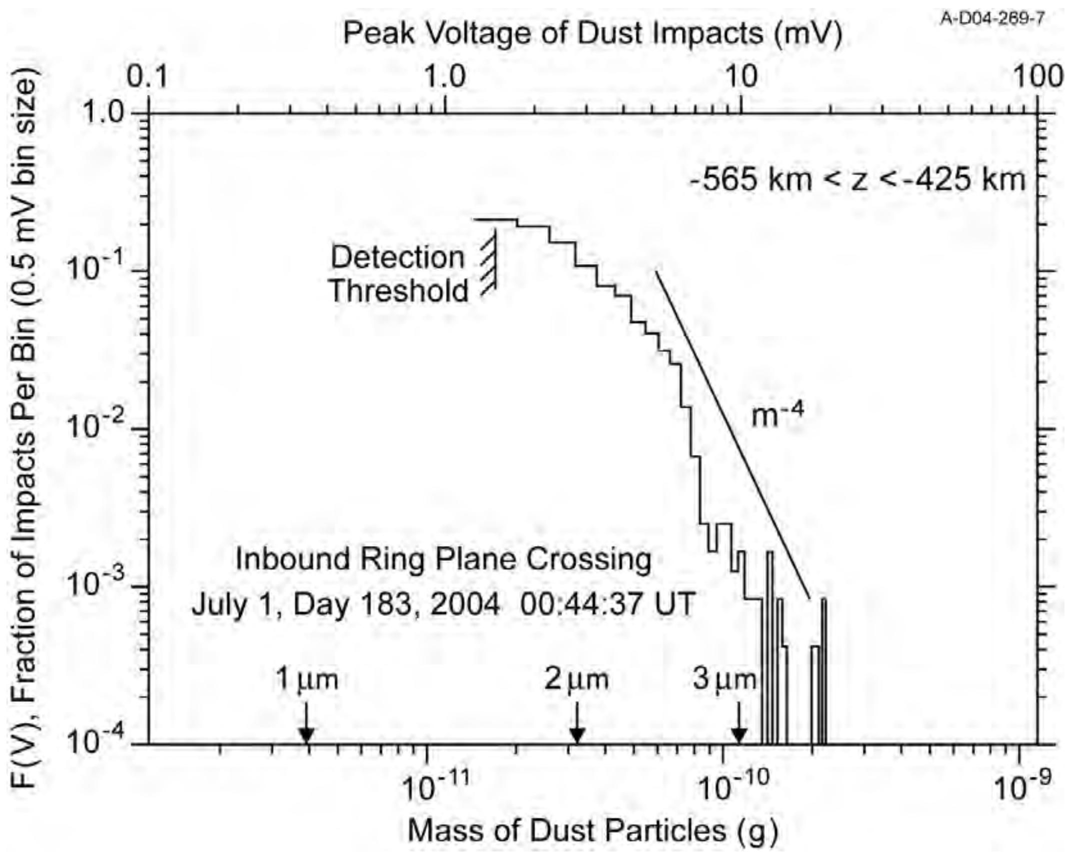

Figure A8. The amplitude distribution of the peak voltages of dust impacts observed south of the first ring plane crossing, at −565 km < z < −425 km. Above about 1 mV, the differential mass distribution dN/dm varies approximately as m^{-4}, indicating that there are proportionally fewer large particles in this region, compared to the region near the center of the ring plane.

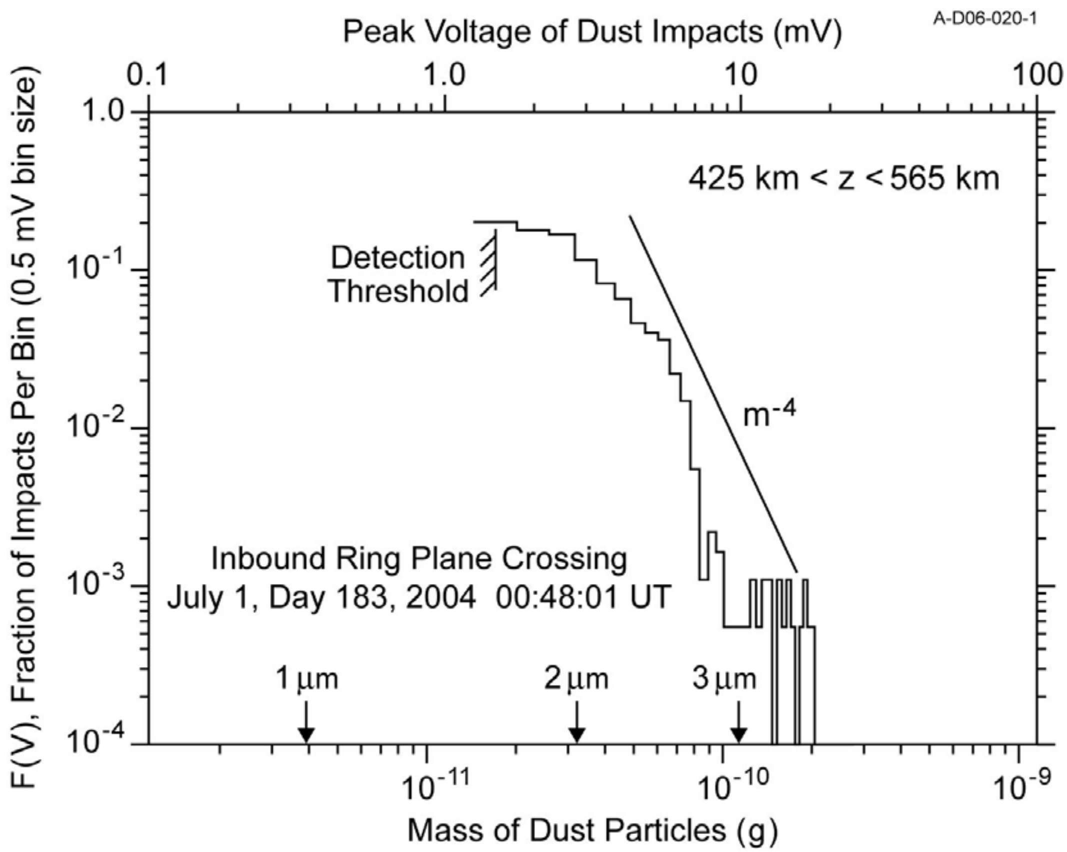

Figure A9. The amplitude distribution of the peak voltages of dust impacts observed north of the center of the first ring plane crossing, for 425 km < z < 565 km. Note the very close similarity to Figure 7, including the step-like decrease at about 8 mV.

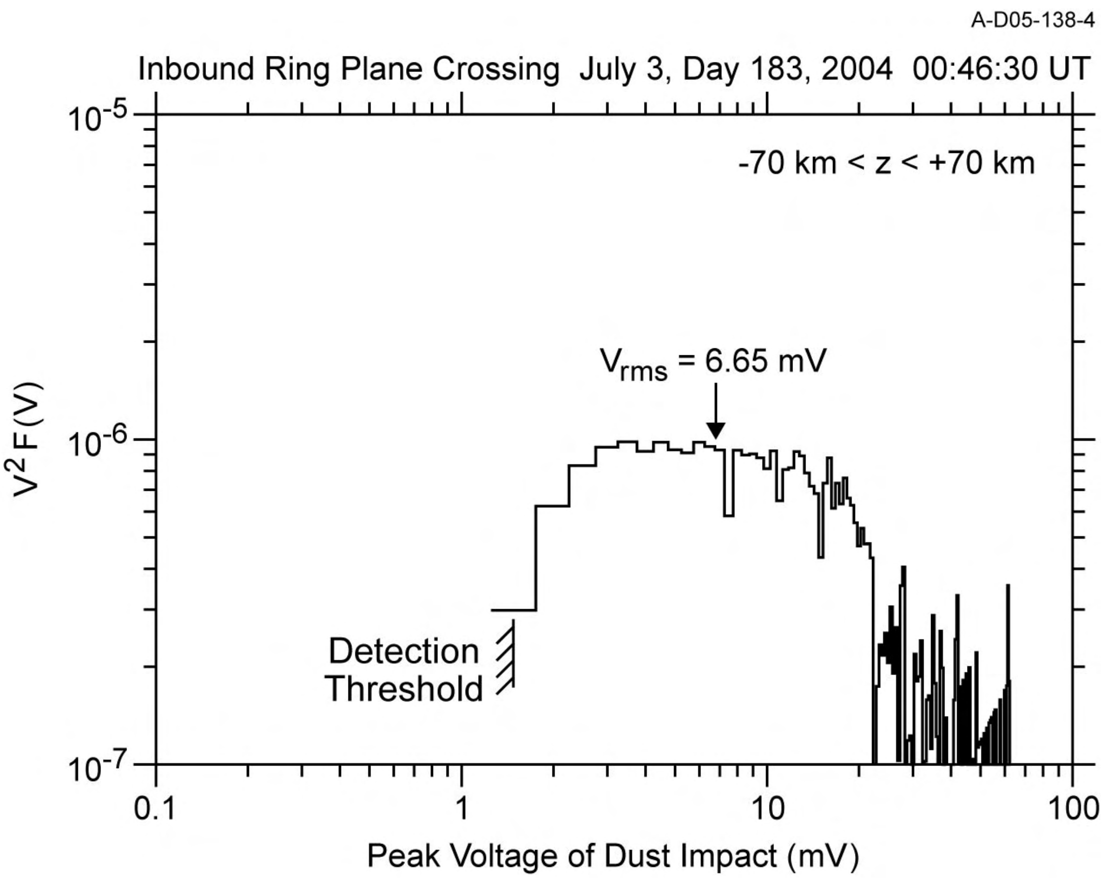

Figure A10. The mass distribution of dust particles near the center of the first ring plane crossing for −70 km < z < 70 km. The quantity $V^2F(V)$ represents the contribution of dust particles to the total r.m.s. voltage, and therefore to the total r.m.s. mass. Note that most of the contribution to the total r.m.s. voltage lies well within the dynamic range of the instrument at this gain setting, i.e., from about 1.6 to 65 mV.

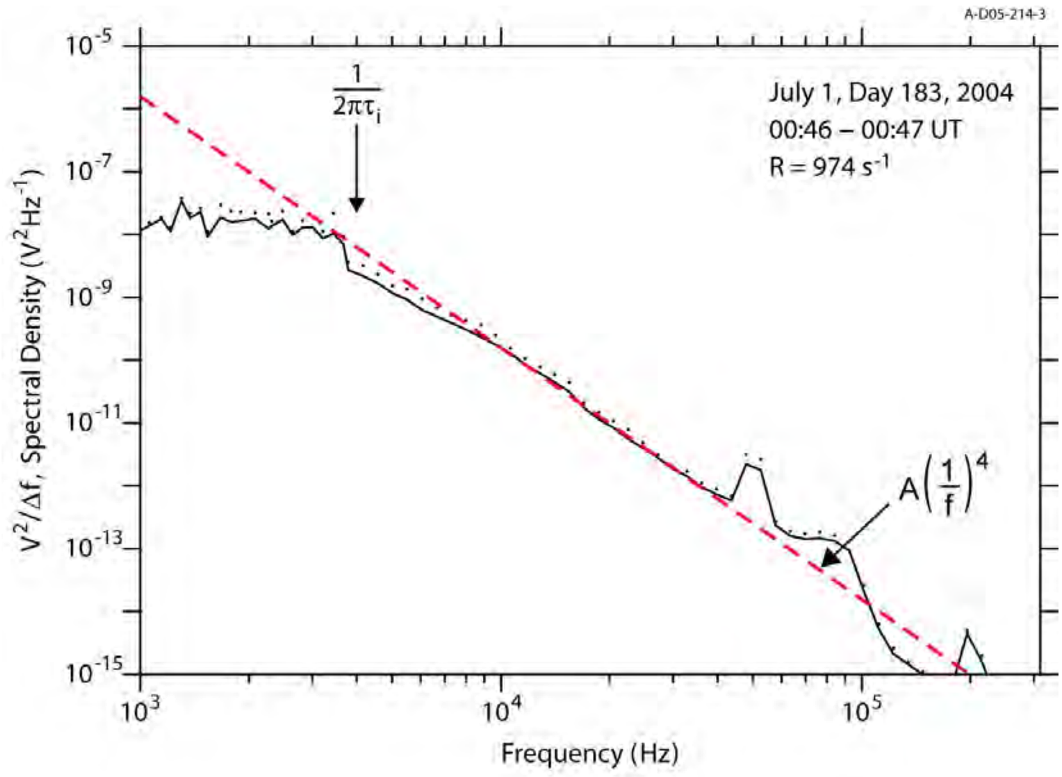

Figure A11. The voltage spectral density of the dust impacts detected by the monopole antenna near the center of the first ring plane crossing. The spectrum varies approximately as f^{-2} at frequencies lower than 4000 Hz and as approximately f^{-4} at frequencies higher than 4000 Hz. The change in slope at $f_c = (1/2\pi\tau)$ provides a useful parameter for estimating the particle mass, and the red line gives the best fit to the f^{-4} part of the spectrum.

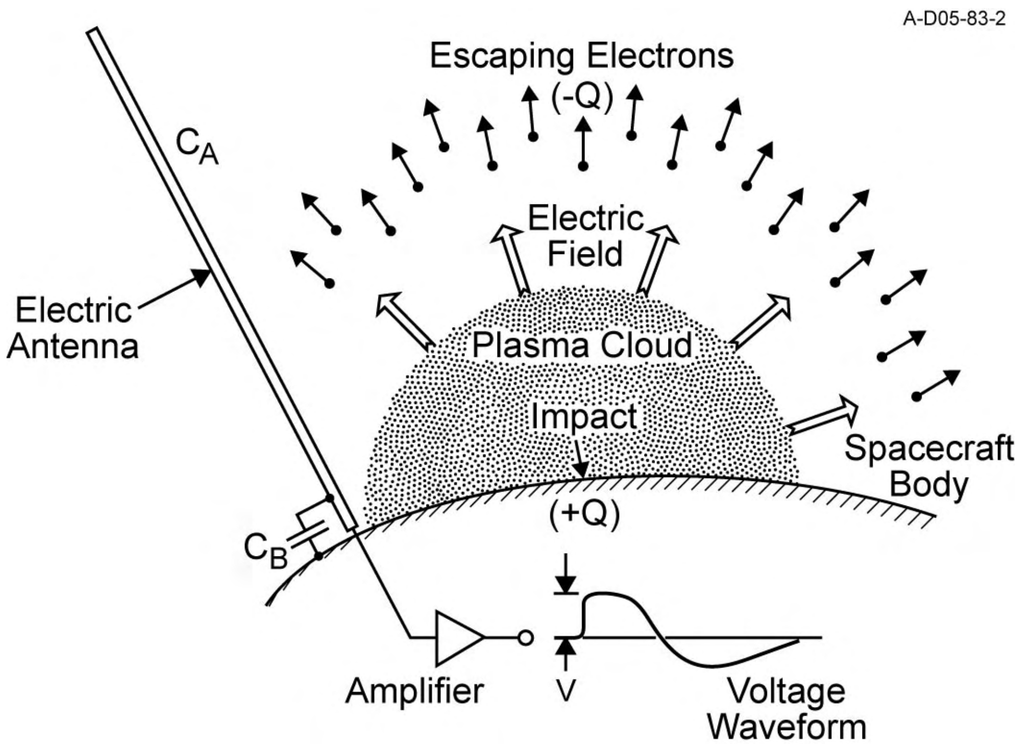

Figure A12. An illustration showing the plasma cloud and the escaping electrons (-Q) produced by an impact on the spacecraft body, and the resulting polarization charge (+Q) on the spacecraft body. The escaping electrons produce a polarization electric field that is detected by the antenna. The resulting antenna voltage is $V = \beta Q/C$, where C is the capacitance of the spacecraft and $\beta \approx 0.4$ is a factor that takes into account the voltage reduction caused by the base capacity of the antenna.

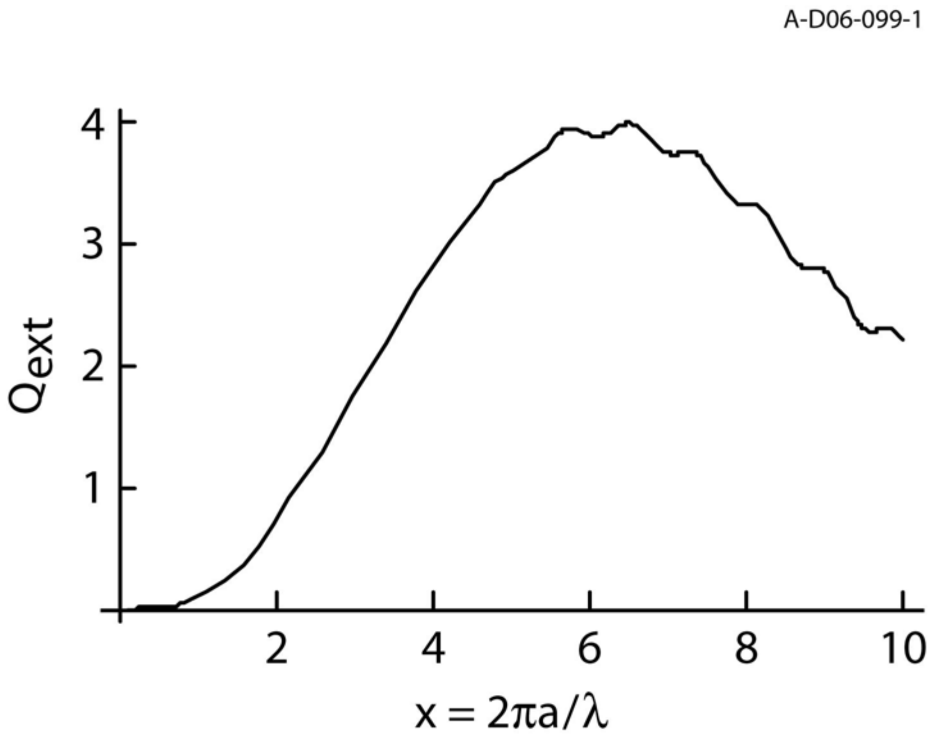

Figure A13. The curve shows Q_{ext}, the extinction efficiency for sphere with the relative refractive m=1.33. x is the ratio of the sphere’s circumference to the wavelength of the incident light.

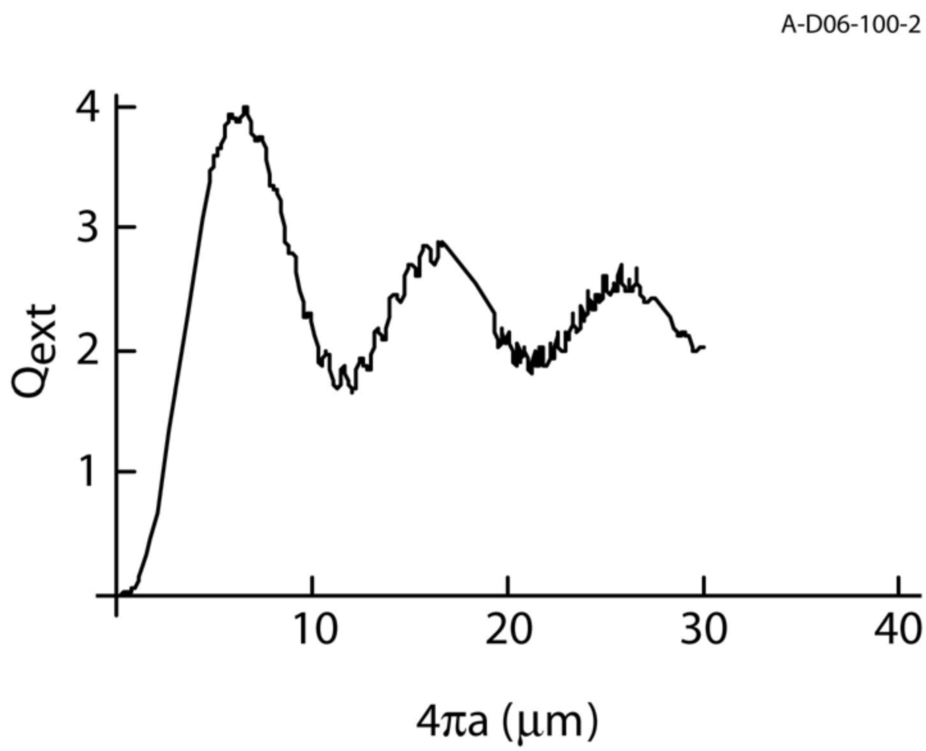

Figure A14. The curve shows Q_{ext} , the extinction efficiency for sphere with the relative refractive m=1.33 as a function of particle size a. as $\lambda = 500nm$.

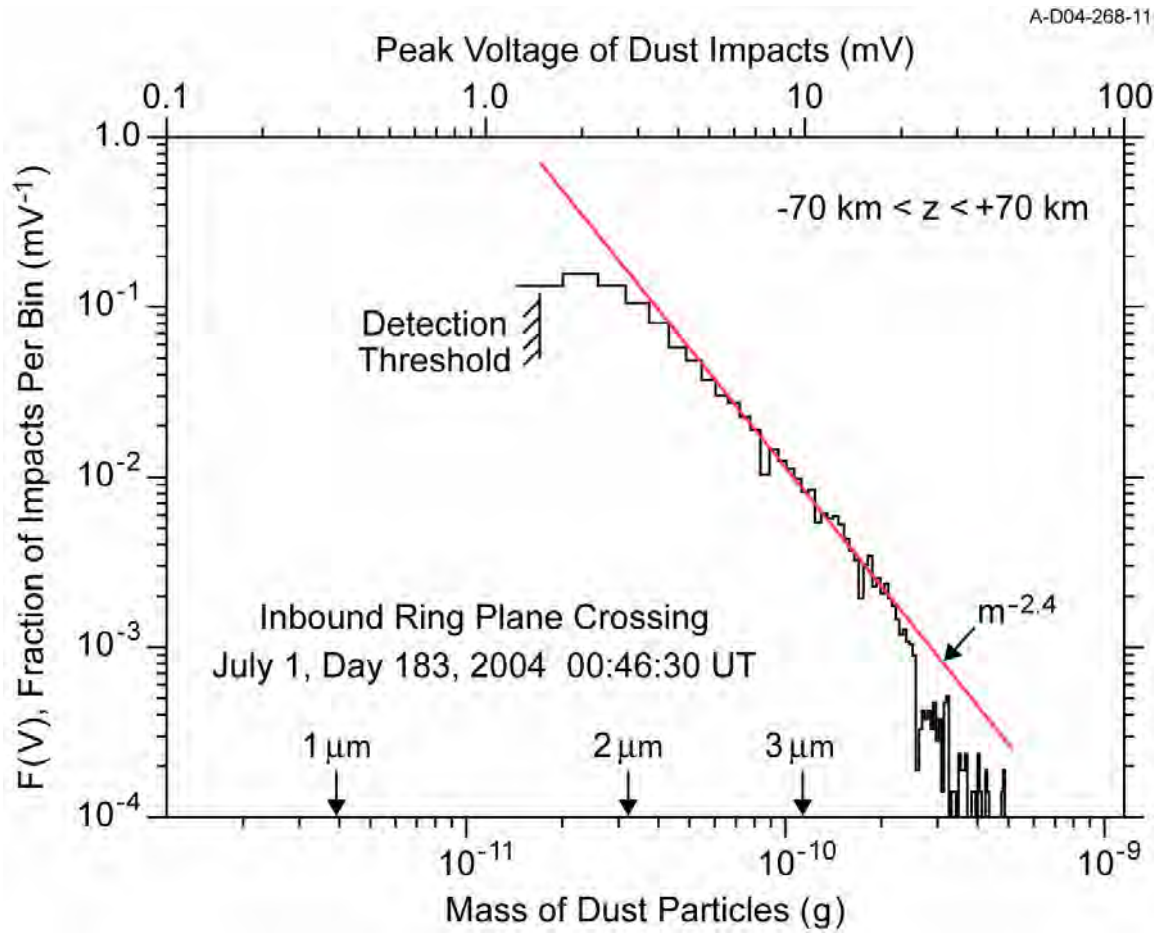

Figure A15. The amplitude distribution of the peak voltage of dust impacts observed near the center of the first ring plane crossing (−70 km < z < 70 km). The fraction of impacts per bin, F(V), is proportional to the differential mass distribution, dN/dm, and the peak voltage of dust impacts is proportional to the mass of the dust particles. Above about 1 mV, the differential mass distribution dN/dm varies approximately as $m^{-2.4}$.

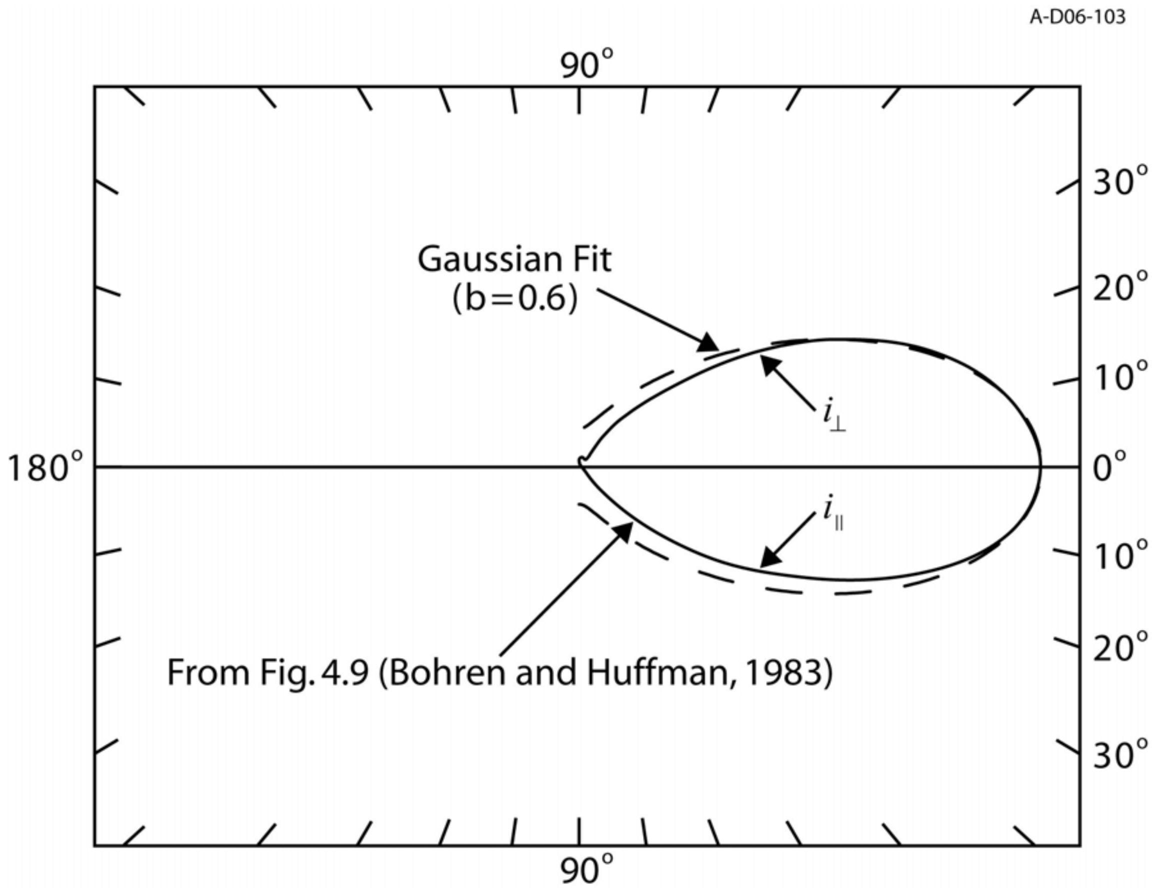

Figure A16. The solid curve shows the normalized scattered light intensity given by as a function of the angle from the incident beam for $x = 2\pi a/\lambda = 3$. The curve labeled $i_\perp$ is in the plane perpendicular to the plane of polarization, and $i_\parallel$ is in the plane of polarization. The dashed line is the best fit Gaussian given by equation (31) with b = 0.6.

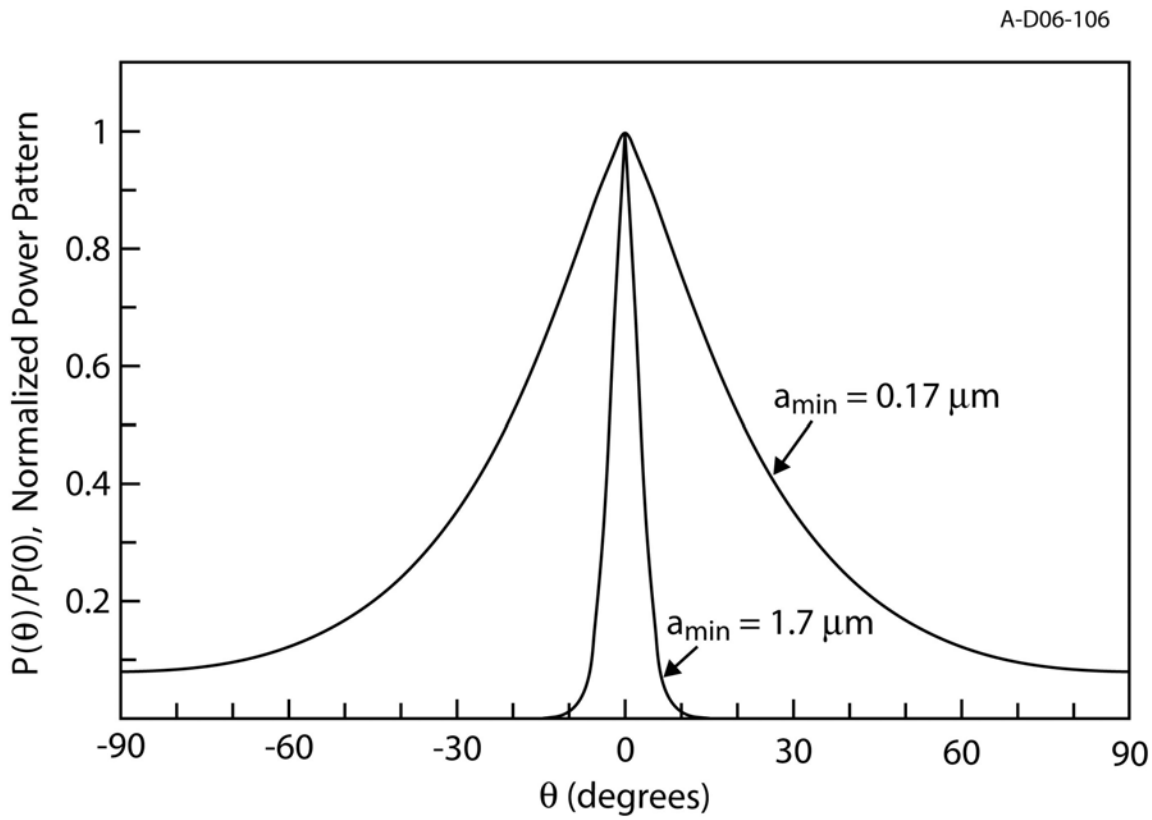

Figure A17. The normalized scattered power pattern as function of the angle, θ, relative to the incident light. The line marked $a_{min} = 1.7\mu m$ represents the angular distribution of scattered light due to dust particles that can be detected by RPWS and gives FWHM of 9°. The line marked $a_{min} = 0.17\mu m$ represents the angular distribution of scattered light for a particle size distribution extended to a lower limit by a factor of 10.

APPENDIX B

VALUES OF EXTINCTION EFFICIENCY

$x = 2\pi a/\lambda$	n_{Max}, Maximum Value of Summation: 4	10	20	30	100
0.1	0.000242	0.000242	0.000242	0.000242	0.000242
0.2	0.003753	0.003753	0.003753	0.003753	0.003753
0.3	0.01809	0.01809	0.01809	0.01809	0.01809
0.4	0.05357	0.05357	0.05357	0.05357	0.05357
0.5	0.120906	0.120906	0.120906	0.120906	0.120906
0.6	0.229281	0.229281	0.229281	0.229281	0.229281
0.7	0.385188	0.385188	0.385188	0.385188	0.385188
0.8	0.591923	0.591923	0.591923	0.591923	0.591923
0.9	0.849423	0.849423	0.849423	0.849423	0.849423
1	1.15422	1.15422	1.15422	1.15422	1.15422
1.5	3.06205	3.06205	3.06205	3.06205	3.06205
2	4.72013	4.72014	4.72014	4.72014	4.72014
2.5	5.95822	5.95824	5.95824	5.95824	5.95824
3	6.91028	6.91076	6.91076	6.91076	6.91076
3.5	7.67797	7.68337	7.68337	7.68337	7.68337
4	8.19403	8.23062	8.23062	8.23062	8.23062
4.5	8.60461	8.77818	8.77818	8.77818	8.77818
5	8.66948	9.31317	9.31317	9.31317	9.31317
5.5	8.03465	9.79982	9.79982	9.79982	9.79982
6	6.77468	9.9919	9.9919	9.9919	9.9919
6.5	5.26558	9.99755	9.99755	9.99755	9.99755
7	3.79688	9.70844	9.70844	9.70844	9.70844
7.5	2.66893	9.42015	9.42017	9.42017	9.42017
8	1.88921	8.8995	8.89963	8.89963	8.89963
8.5	1.45315	8.48851	8.48929	8.48929	8.48929
9	1.22385	7.99249	7.99671	7.99671	7.99671
9.5	1.10621	7.45281	7.47301	7.47301	7.47301
10	0.950657	7.05638	7.15439	7.15439	7.15439
11	0.670166	5.0985	6.57165	6.57165	6.57165
12	0.903229	4.08172	6.37292	6.37292	6.37292
13	1.18	3.77088	6.57192	6.57192	6.57192
14	1.12331	3.94573	7.14693	7.14693	7.14693
15	0.922345	4.28562	7.95455	7.95455	7.95455

APPENDIX C

CODE FOR OPTICAL PROPERTIES

```
SphericalBesselJ[n_, x_] = Sqrt[π/(2*x)] BesselJ[n + 1/2, x];

SphericalBesselY[n_, x_] = Sqrt[π/(2*x)] BesselY[n + 1/2, x];

SphericalHankelH[n_,x_]=SphericalBesselJ[n,x]+i SphericalBesselY[n,x];

RicBesselΨ[n_,x_]=x SphericalBesselJ[n,x];

RicBesselζ[n_,x_]=x SphericalHankelH[n,x];

DRicBesselΨ[n_,x_]=D[RicBesselΨ[n,x],x];

DRicBesselζ[n_,x_]=D[RicBesselζ[n,x],x];

m=1.33;

a[n_,x_]=(m*RicBesselΨ[n,m*x] DRicBesselΨ[n,x]-RicBesselΨ[n,x]
DRicBesselΨ[n,m*x])/(m*RicBesselΨ[n,m*x] DRicBesselζ[n,x]-RicBesselζ[n,x]
DRicBesselΨ[n,m*x]);

b[n_,x_]=(RicBesselΨ[n,m*x]*DRicBesselΨ[n,x]-m*RicBesselΨ[n,x]
*DRicBesselΨ[n,m*x])/(RicBesselΨ[n,m*x]*DRicBesselζ[n,x]-m*RicBesselζ[n,x]
DRicBesselΨ[n,m*x]);

Qext[x_] = (1/(π ((x*λ)/(2π))^2)) * ((2π)/(2π/λ)^2) * Sum[(2 n + 1) * ((Abs[a[n, x]])^2
    + (Abs[b[n, x]])^2), {n, 1, 30}];

Plot[Qext[x],{x,0.1,10},AxesLabel→TraditionalForm/@{2πa/λ,Qext},
TextStyle→{FontFamily→"Times",FontSize→14},PlotStyle→{Hue[0.8]}]
```

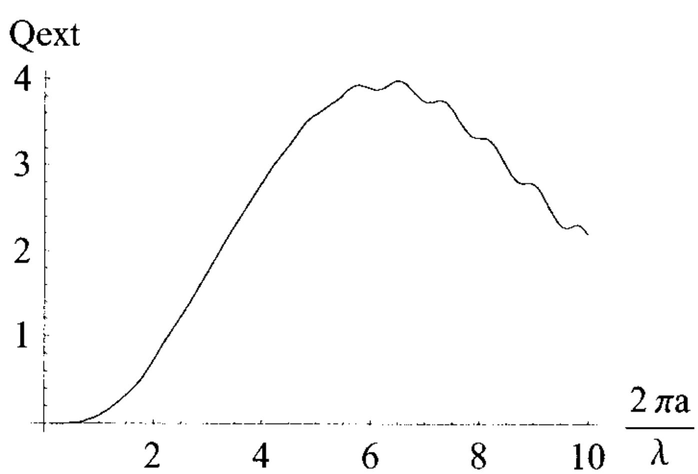

- Graphics -

```
Plot[Qext[x], {x, 0.1, 30}, AxesLabel → TraditionalForm /@ {2 πa / λ, Qext},
  TextStyle → {FontFamily → "Times", FontSize → 14}, PlotStyle → {Hue[0.8]}]
```

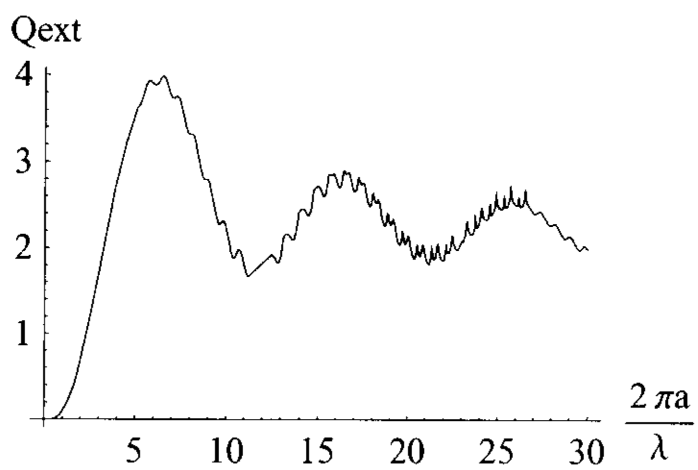

- Graphics -

```
Tao[x_] = Qext[x] * (x^-3.2);

Bb[x_]=Exp[-x^2/1.884^2]*(1.884/x)*N[Erfi[x/1.884]];

Shidi[x_]=Exp[-((x^2)*(Sin[π*k/60]^2))/1.884^2];

Pp[x_]=Bb[x]*Shidi[x];
```

```
M = Table[{π * k / 60, (N[Log[Sum[Pp[x] * 0.1, {x, 21.0, 73.0, 0.1}]]]
        + 2.683833575279646`)}, {k, -30, 30, 1}]
```

$\{\{-\frac{\pi}{2}, -128.894\}, \{-\frac{29\pi}{60}, -128.553\}, \{-\frac{7\pi}{15}, -127.531\}, \{-\frac{9\pi}{20}, -125.841\}, \{-\frac{13\pi}{30}, -123.501\},$
$\{-\frac{5\pi}{12}, -120.535\}, \{-\frac{2\pi}{5}, -116.977\}, \{-\frac{23\pi}{60}, -112.864\}, \{-\frac{11\pi}{30}, -108.242\}, \{-\frac{7\pi}{20}, -103.16\},$
$\{-\frac{\pi}{3}, -97.6721\}, \{-\frac{19\pi}{60}, -91.8388\}, \{-\frac{3\pi}{10}, -85.7225\}, \{-\frac{17\pi}{60}, -79.3889\}, \{-\frac{4\pi}{15}, -72.9059\},$
$\{-\frac{\pi}{4}, -66.3427\}, \{-\frac{7\pi}{30}, -59.7694\}, \{-\frac{13\pi}{60}, -53.2557\}, \{-\frac{\pi}{5}, -46.87\}, \{-\frac{11\pi}{60}, -40.6793\},$
$\{-\frac{\pi}{6}, -34.7476\}, \{-\frac{3\pi}{20}, -29.1351\}, \{-\frac{2\pi}{15}, -23.8977\}, \{-\frac{7\pi}{60}, -19.0856\}, \{-\frac{\pi}{10}, -14.7425\},$
$\{-\frac{\pi}{12}, -10.904\}, \{-\frac{\pi}{15}, -7.59572\}, \{-\frac{\pi}{20}, -4.83118\}, \{-\frac{\pi}{30}, -2.60778\}, \{-\frac{\pi}{60}, -0.903329\},$
$\{0, 0.\}, \{\frac{\pi}{60}, -0.903329\}, \{\frac{\pi}{30}, -2.60778\}, \{\frac{\pi}{20}, -4.83118\}, \{\frac{\pi}{15}, -7.59572\}, \{\frac{\pi}{12}, -10.904\},$
$\{\frac{\pi}{10}, -14.7425\}, \{\frac{7\pi}{60}, -19.0856\}, \{\frac{2\pi}{15}, -23.8977\}, \{\frac{3\pi}{20}, -29.1351\}, \{\frac{\pi}{6}, -34.7476\},$
$\{\frac{11\pi}{60}, -40.6793\}, \{\frac{\pi}{5}, -46.87\}, \{\frac{13\pi}{60}, -53.2557\}, \{\frac{7\pi}{30}, -59.7694\}, \{\frac{\pi}{4}, -66.3427\},$
$\{\frac{4\pi}{15}, -72.9059\}, \{\frac{17\pi}{60}, -79.3889\}, \{\frac{3\pi}{10}, -85.7225\}, \{\frac{19\pi}{60}, -91.8388\}, \{\frac{\pi}{3}, -97.6721\},$
$\{\frac{7\pi}{20}, -103.16\}, \{\frac{11\pi}{30}, -108.242\}, \{\frac{23\pi}{60}, -112.864\}, \{\frac{2\pi}{5}, -116.977\}, \{\frac{5\pi}{12}, -120.535\},$
$\{\frac{13\pi}{30}, -123.501\}, \{\frac{9\pi}{20}, -125.841\}, \{\frac{7\pi}{15}, -127.531\}, \{\frac{29\pi}{60}, -128.553\}, \{\frac{\pi}{2}, -128.894\}\}$

```
ListPlot[M, PlotJoined → True, AxesLabel → TraditionalForm /@ {θ, lnP (θ)},
  TextStyle → {FontFamily → "Times", FontSize → 14}, PlotStyle → {Hue[0.85]}]
```

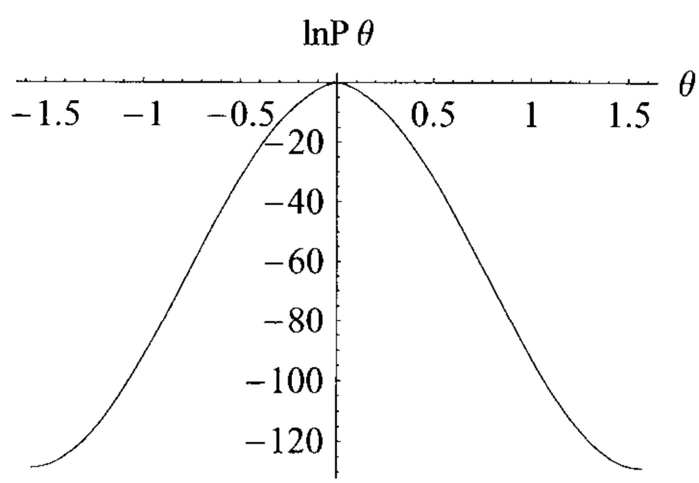

- Graphics -

```
MM = Table[{π * k / 60, N[Sum[Pp[x] * 0.1, {x, 21.0, 73.0, 0.1}]]
     / 0.06830081531055472`}, {k, -8, 8, 1}]
```

$\{\{-\frac{2\pi}{15}, 4.18197\times10^{-11}\}, \{-\frac{7\pi}{60}, 5.14311\times10^{-9}\}, \{-\frac{\pi}{10}, 3.95733\times10^{-7}\}, \{-\frac{\pi}{12}, 0.000018385\}, \{-\frac{\pi}{15}, 0.000502598\}, \{-\frac{\pi}{20}, 0.00797712\}, \{-\frac{\pi}{30}, 0.0736977\}, \{-\frac{\pi}{60}, 0.405218\}, \{0, 1.\}, \{\frac{\pi}{60}, 0.405218\}, \{\frac{\pi}{30}, 0.0736977\}, \{\frac{\pi}{20}, 0.00797712\}, \{\frac{\pi}{15}, 0.000502598\}, \{\frac{\pi}{12}, 0.000018385\}, \{\frac{\pi}{10}, 3.95733\times10^{-7}\}, \{\frac{7\pi}{60}, 5.14311\times10^{-9}\}, \{\frac{2\pi}{15}, 4.18197\times10^{-11}\}\}$

```
ListPlot[MM, PlotJoined → True, AxesLabel → TraditionalForm /@ {θ, P (θ)},
  TextStyle → {FontFamily → "Times", FontSize → 14}, PlotStyle → {Hue[0.85]}]
```

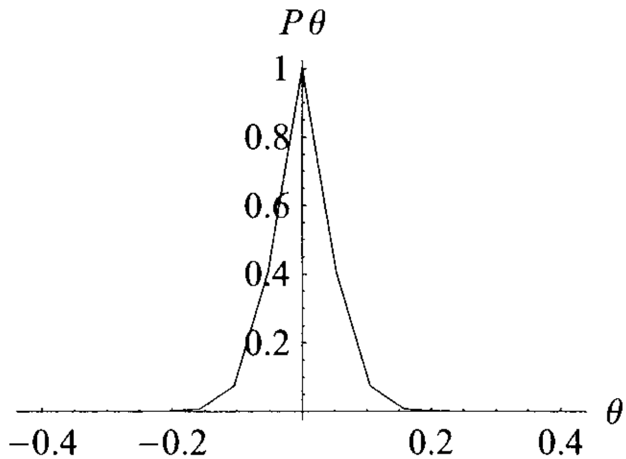

- Graphics -

```
M2 = Table[{π * k / 60, N[Log[Sum[Pp[x] * 0.1,
        {x, 2.1, 73.0, 0.1}]]] - 0.0851242775957501`}, {k, -30, 30, 1}]
```

$$\{\{-\frac{\pi}{2}, -2.60375\}, \{-\frac{29\pi}{60}, -2.59884\}, \{-\frac{7\pi}{15}, -2.58417\}, \{-\frac{9\pi}{20}, -2.55984\}, \{-\frac{13\pi}{30}, -2.52601\},$$
$$\{-\frac{5\pi}{12}, -2.48293\}, \{-\frac{2\pi}{5}, -2.4309\}, \{-\frac{23\pi}{60}, -2.37029\}, \{-\frac{11\pi}{30}, -2.30152\}, \{-\frac{7\pi}{20}, -2.22506\},$$
$$\{-\frac{\pi}{3}, -2.14145\}, \{-\frac{19\pi}{60}, -2.05126\}, \{-\frac{3\pi}{10}, -1.95509\}, \{-\frac{17\pi}{60}, -1.85358\}, \{-\frac{4\pi}{15}, -1.74742\},$$
$$\{-\frac{\pi}{4}, -1.63728\}, \{-\frac{7\pi}{30}, -1.52388\}, \{-\frac{13\pi}{60}, -1.40794\}, \{-\frac{\pi}{5}, -1.29018\}, \{-\frac{11\pi}{60}, -1.17131\},$$
$$\{-\frac{\pi}{6}, -1.05207\}, \{-\frac{3\pi}{20}, -0.933127\}, \{-\frac{2\pi}{15}, -0.815175\}, \{-\frac{7\pi}{60}, -0.698856\}, \{-\frac{\pi}{10}, -0.584782\},$$
$$\{-\frac{\pi}{12}, -0.473519\}, \{-\frac{\pi}{15}, -0.365581\}, \{-\frac{\pi}{20}, -0.261423\}, \{-\frac{\pi}{30}, -0.161432\}, \{-\frac{\pi}{60}, -0.0659634\},$$
$$\{0, 0.\}, \{\frac{\pi}{60}, -0.0659634\}, \{\frac{\pi}{30}, -0.161432\}, \{\frac{\pi}{20}, -0.261423\}, \{\frac{\pi}{15}, -0.365581\}, \{\frac{\pi}{12}, -0.473519\},$$
$$\{\frac{\pi}{10}, -0.584782\}, \{\frac{7\pi}{60}, -0.698856\}, \{\frac{2\pi}{15}, -0.815175\}, \{\frac{3\pi}{20}, -0.933127\}, \{\frac{\pi}{6}, -1.05207\},$$
$$\{\frac{11\pi}{60}, -1.17131\}, \{\frac{\pi}{5}, -1.29018\}, \{\frac{13\pi}{60}, -1.40794\}, \{\frac{7\pi}{30}, -1.52388\}, \{\frac{\pi}{4}, -1.63728\},$$
$$\{\frac{4\pi}{15}, -1.74742\}, \{\frac{17\pi}{60}, -1.85358\}, \{\frac{3\pi}{10}, -1.95509\}, \{\frac{19\pi}{60}, -2.05126\}, \{\frac{\pi}{3}, -2.14145\},$$
$$\{\frac{7\pi}{20}, -2.22506\}, \{\frac{11\pi}{30}, -2.30152\}, \{\frac{23\pi}{60}, -2.37029\}, \{\frac{2\pi}{5}, -2.4309\}, \{\frac{5\pi}{12}, -2.48293\},$$
$$\{\frac{13\pi}{30}, -2.52601\}, \{\frac{9\pi}{20}, -2.55984\}, \{\frac{7\pi}{15}, -2.58417\}, \{\frac{29\pi}{60}, -2.59884\}, \{\frac{\pi}{2}, -2.60375\}\}$$

```
ListPlot[M2, PlotJoined → True, AxesLabel → TraditionalForm /@ {θ, lnP (θ)},
  TextStyle → {FontFamily → "Times", FontSize → 14}, PlotStyle → {Hue[0.85]}]
```

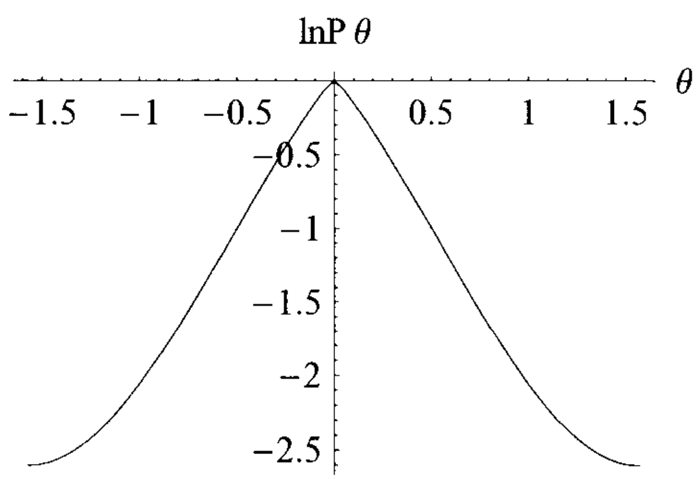

- Graphics -

MM2 = Table[{π * k / 60, N[Sum[Pp[x] * 0.1, {x, 2.1, 73.0, 0.1}]] / 1.0888523782458228`}, {k, −30, 30, 1}]

$\{\{-\frac{\pi}{2}, 0.0739959\}, \{-\frac{29\pi}{60}, 0.0743595\}, \{-\frac{7\pi}{15}, 0.0754585\}, \{-\frac{9\pi}{20}, 0.0773175\}, \{-\frac{13\pi}{30}, 0.0799777\},$
$\{-\frac{5\pi}{12}, 0.0834985\}, \{-\frac{2\pi}{5}, 0.0879578\}, \{-\frac{23\pi}{60}, 0.0934539\}, \{-\frac{11\pi}{30}, 0.100107\}, \{-\frac{7\pi}{20}, 0.108061\},$
$\{-\frac{\pi}{3}, 0.117484\}, \{-\frac{19\pi}{60}, 0.128573\}, \{-\frac{3\pi}{10}, 0.141552\}, \{-\frac{17\pi}{60}, 0.156675\}, \{-\frac{4\pi}{15}, 0.174223\},$
$\{-\frac{\pi}{4}, 0.194508\}, \{-\frac{7\pi}{30}, 0.217865\}, \{-\frac{13\pi}{60}, 0.244647\}, \{-\frac{\pi}{5}, 0.275222\}, \{-\frac{11\pi}{60}, 0.309959\},$
$\{-\frac{\pi}{6}, 0.349216\}, \{-\frac{3\pi}{20}, 0.393322\}, \{-\frac{2\pi}{15}, 0.442562\}, \{-\frac{7\pi}{60}, 0.497154\}, \{-\frac{\pi}{10}, 0.557228\},$
$\{-\frac{\pi}{12}, 0.622807\}, \{-\frac{\pi}{15}, 0.693793\}, \{-\frac{\pi}{20}, 0.769955\}, \{-\frac{\pi}{30}, 0.850924\}, \{-\frac{\pi}{60}, 0.936165\},$
$\{0, 1.\}, \{\frac{\pi}{60}, 0.936165\}, \{\frac{\pi}{30}, 0.850924\}, \{\frac{\pi}{20}, 0.769955\}, \{\frac{\pi}{15}, 0.693793\}, \{\frac{\pi}{12}, 0.622807\},$
$\{\frac{\pi}{10}, 0.557228\}, \{\frac{7\pi}{60}, 0.497154\}, \{\frac{2\pi}{15}, 0.442562\}, \{\frac{3\pi}{20}, 0.393322\}, \{\frac{\pi}{6}, 0.349216\},$
$\{\frac{11\pi}{60}, 0.309959\}, \{\frac{\pi}{5}, 0.275222\}, \{\frac{13\pi}{60}, 0.244647\}, \{\frac{7\pi}{30}, 0.217865\}, \{\frac{\pi}{4}, 0.194508\},$
$\{\frac{4\pi}{15}, 0.174223\}, \{\frac{17\pi}{60}, 0.156675\}, \{\frac{3\pi}{10}, 0.141552\}, \{\frac{19\pi}{60}, 0.128573\}, \{\frac{\pi}{3}, 0.117484\},$
$\{\frac{7\pi}{20}, 0.108061\}, \{\frac{11\pi}{30}, 0.100107\}, \{\frac{23\pi}{60}, 0.0934539\}, \{\frac{2\pi}{5}, 0.0879578\}, \{\frac{5\pi}{12}, 0.0834985\},$
$\{\frac{13\pi}{30}, 0.0799777\}, \{\frac{9\pi}{20}, 0.0773175\}, \{\frac{7\pi}{15}, 0.0754585\}, \{\frac{29\pi}{60}, 0.0743595\}, \{\frac{\pi}{2}, 0.0739959\}\}$

```
ListPlot[MM2, PlotJoined → True, AxesOrigin → {0, 0},
  PlotRange → {0, 1.1}, AxesLabel → TraditionalForm /@ {θ, P (θ)},
  TextStyle → {FontFamily → "Times", FontSize → 14}, PlotStyle → {Hue[0.85]}]
```

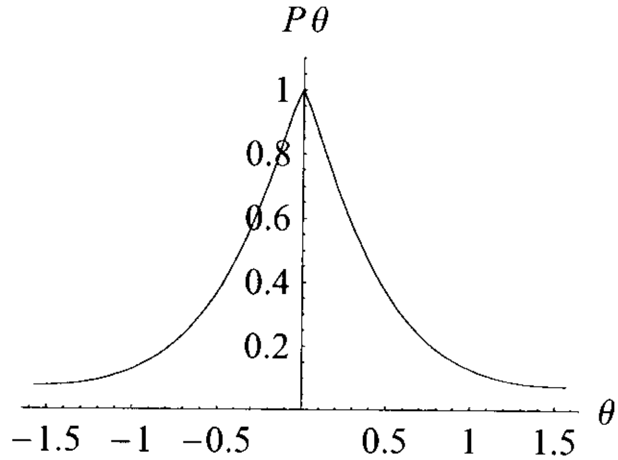

- Graphics -

```
W2[x_] = Qext[x] * (x^(-3.2)) * (2.066 * (10^(-24)))
 * ((4 * Pi * 10^4)^2.2) * Pi * (4.17 * 10^7);
Sum[W2[x] * 0.1, {x, 21, 73.0, 0.1}]
MD2 = {{0.1`, 0.0000143947884784283`}, {1.1`, 0.0000116014267413929 8`},
   {2.1`, 7.724516928423199`*^-6}, {3.1`, 4.874488066757301`*^-6},
   {4.1`, 3.037840880325285`*^-6}, {5.1`, 1.8787686167025816`*^-6},
   {6.1`, 1.161837430803193`*^-6}, {7.1`, 7.306784022987921`*^-7},
   {8.1`, 4.797204413062463`*^-7}, {9.1`, 3.379129611751039`*^-7},
   {10.1`, 2.5874295792581223`*^-7}, {11.1`, 2.124845059779978`*^-7},
   {12.1`, 1.8130828545076266`*^-7}, {13.1`, 1.5589796660695908`*^-7},
   {14.1`, 1.325984652184506`*^-7}, {15.1`, 1.1119461073526631`*^-7},
   {16.1`, 9.230909869810797`*^-8}, {17.1`, 7.660668852992074`*^-8},
   {18.1`, 6.41505793982074`*^-8}, {19.1`, 5.4686213753723516`*^-8},
   {20.1`, 4.75763463915502`*^-8}, {21.1`, 4.2079936190758037`*^-8},
   {22.1`, 3.748008023285553`*^-8}, {23.1`, 3.3239605304264474`*^-8},
   {24.1`, 2.92119193358042`*^-8}, {25.1`, 2.534575572373891`*^-8},
   {26.1`, 2.1818596678179065`*^-8}, {27.1`, 1.8719587291359305`*^-8},
   {28.1`, 1.6121682968070294`*^-8}, {29.1`, 1.3967123569700123`*^-8},
   {30.1`, 1.2178407005952725`*^-8}}
ListPlot[MD2, PlotJoined → True, AxesLabel → TraditionalForm /@ {k, OD},
  TextStyle → {FontFamily → "Times", FontSize → 14}, PlotStyle → {Hue[0.85]}]
```

$\{4.25694\times 10^{-8}\}$

$\{\{0.1, 0.0000143948\}, \{1.1, 0.0000116014\}, \{2.1, 7.72452\times 10^{-6}\}, \{3.1, 4.87449\times 10^{-6}\}, \{4.1, 3.03784\times 10^{-6}\}, \{5.1, 1.87877\times 10^{-6}\}, \{6.1, 1.16184\times 10^{-6}\}, \{7.1, 7.30678\times 10^{-7}\}, \{8.1, 4.7972\times 10^{-7}\}, \{9.1, 3.37913\times 10^{-7}\}, \{10.1, 2.58743\times 10^{-7}\}, \{11.1, 2.12485\times 10^{-7}\}, \{12.1, 1.81308\times 10^{-7}\}, \{13.1, 1.55898\times 10^{-7}\}, \{14.1, 1.32598\times 10^{-7}\}, \{15.1, 1.11195\times 10^{-7}\}, \{16.1, 9.23091\times 10^{-8}\}, \{17.1, 7.66067\times 10^{-8}\}, \{18.1, 6.41506\times 10^{-8}\}, \{19.1, 5.46862\times 10^{-8}\}, \{20.1, 4.75763\times 10^{-8}\}, \{21.1, 4.20799\times 10^{-8}\}, \{22.1, 3.74801\times 10^{-8}\}, \{23.1, 3.32396\times 10^{-8}\}, \{24.1, 2.92119\times 10^{-8}\}, \{25.1, 2.53458\times 10^{-8}\}, \{26.1, 2.18186\times 10^{-8}\}, \{27.1, 1.87196\times 10^{-8}\}, \{28.1, 1.61217\times 10^{-8}\}, \{29.1, 1.39671\times 10^{-8}\}, \{30.1, 1.21784\times 10^{-8}\}\}$

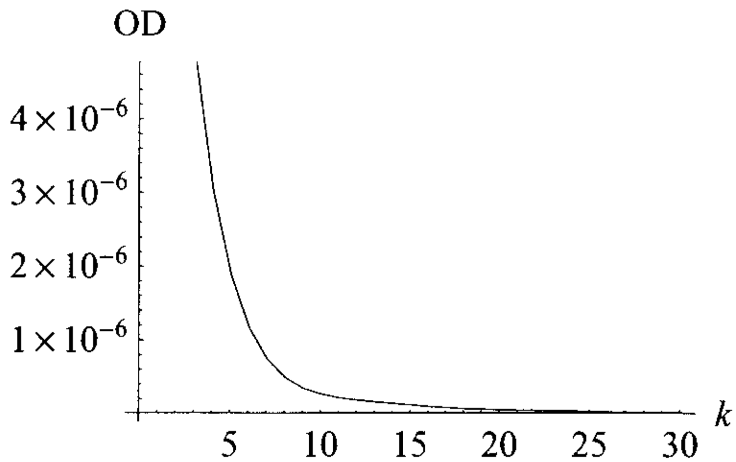

- Graphics -

```
Sum[W2[x] * 0.1, {x, 21.0, 73.0, 0.1}]
```

$\{4.25694 \times 10^{-8}\}$

$$MM3 = \{\{-\frac{\pi}{2}, 0\}, \{-\frac{29\pi}{60}, 0\}, \{-\frac{7\pi}{15}, 0\}, \{-\frac{9\pi}{20}, 0\}, \{-\frac{13\pi}{30}, 0\}, \{-\frac{5\pi}{12}, 0\}, \{-\frac{2\pi}{5}, 0\}, \{-\frac{23\pi}{60}, 0\}, \{-\frac{11\pi}{30}, 0\}, \{-\frac{7\pi}{20}, 0\}, \{-\frac{\pi}{3}, 0\}, \{-\frac{19\pi}{60}, 0\}, \{-\frac{3\pi}{10}, 0\}, \{-\frac{17\pi}{60}, 0\}, \{-\frac{4\pi}{15}, 0\}, \{-\frac{\pi}{4}, 0\}, \{-\frac{7\pi}{30}, 0\}, \{-\frac{13\pi}{60}, 0\}, \{-\frac{\pi}{5}, 0\}, \{-\frac{11\pi}{60}, 0\}, \{-\frac{\pi}{6}, 0\}, \{-\frac{3\pi}{20}, 0\}, \{-\frac{2\pi}{15}, 0\}, \{-\frac{7\pi}{60}, 0\}, \{-\frac{\pi}{10}, 0\}, \{-\frac{\pi}{12}, 0\}, \{-\frac{\pi}{15}, 0.0005025977194427429`\}, \{-\frac{\pi}{20}, 0.00797712462609496`\}, \{-\frac{\pi}{30}, 0.0736976740766175`\}, \{-\frac{\pi}{60}, 0.4052183251618814`\}, \{0, 1.`\}, \{\frac{\pi}{60}, 0.4052183251618814`\}, \{\frac{\pi}{30}, 0.0736976740766175`\}, \{\frac{\pi}{20}, 0.00797712462609496`\}, \{\frac{\pi}{15}, 0.0005025977194427429`\}, \{\frac{\pi}{12}, 0\}, \{\frac{\pi}{10}, 0\}, \{\frac{7\pi}{60}, 0\}, \{\frac{2\pi}{15}, 0\}, \{\frac{3\pi}{20}, 0\}, \{\frac{\pi}{6}, 0\}, \{\frac{11\pi}{60}, 0\}, \{\frac{\pi}{5}, 0\}, \{\frac{13\pi}{60}, 0\}, \{\frac{7\pi}{30}, 0\}, \{\frac{\pi}{4}, 0\}, \{\frac{4\pi}{15}, 0\}, \{\frac{17\pi}{60}, 0\}, \{\frac{3\pi}{10}, 0\}, \{\frac{19\pi}{60}, 0\}, \{\frac{\pi}{3}, 0\}, \{\frac{7\pi}{20}, 0\}, \{\frac{11\pi}{30}, 0\}, \{\frac{23\pi}{60}, 0\}, \{\frac{2\pi}{5}, 0\}, \{\frac{5\pi}{12}, 0\}, \{\frac{13\pi}{30}, 0\}, \{\frac{9\pi}{20}, 0\}, \{\frac{7\pi}{15}, 0\}, \{\frac{29\pi}{60}, 0\}, \{\frac{\pi}{2}, 0\}\}$$

$$\{\{-\frac{\pi}{2}, 0\}, \{-\frac{29\pi}{60}, 0\}, \{-\frac{7\pi}{15}, 0\}, \{-\frac{9\pi}{20}, 0\}, \{-\frac{13\pi}{30}, 0\}, \{-\frac{5\pi}{12}, 0\}, \{-\frac{2\pi}{5}, 0\}, \{-\frac{23\pi}{60}, 0\}, \{-\frac{11\pi}{30}, 0\}, \{-\frac{7\pi}{20}, 0\}, \{-\frac{\pi}{3}, 0\}, \{-\frac{19\pi}{60}, 0\}, \{-\frac{3\pi}{10}, 0\}, \{-\frac{17\pi}{60}, 0\}, \{-\frac{4\pi}{15}, 0\}, \{-\frac{\pi}{4}, 0\}, \{-\frac{7\pi}{30}, 0\}, \{-\frac{13\pi}{60}, 0\}, \{-\frac{\pi}{5}, 0\}, \{-\frac{11\pi}{60}, 0\}, \{-\frac{\pi}{6}, 0\}, \{-\frac{3\pi}{20}, 0\}, \{-\frac{2\pi}{15}, 0\}, \{-\frac{7\pi}{60}, 0\}, \{-\frac{\pi}{10}, 0\}, \{-\frac{\pi}{12}, 0\}, \{-\frac{\pi}{15}, 0.000502598\}, \{-\frac{\pi}{20}, 0.00797712\}, \{-\frac{\pi}{30}, 0.0736977\}, \{-\frac{\pi}{60}, 0.405218\}, \{0, 1.\}, \{\frac{\pi}{60}, 0.405218\}, \{\frac{\pi}{30}, 0.0736977\}, \{\frac{\pi}{20}, 0.00797712\}, \{\frac{\pi}{15}, 0.000502598\}, \{\frac{\pi}{12}, 0\}, \{\frac{\pi}{10}, 0\}, \{\frac{7\pi}{60}, 0\}, \{\frac{2\pi}{15}, 0\}, \{\frac{3\pi}{20}, 0\}, \{\frac{\pi}{6}, 0\}, \{\frac{11\pi}{60}, 0\}, \{\frac{\pi}{5}, 0\}, \{\frac{13\pi}{60}, 0\}, \{\frac{7\pi}{30}, 0\}, \{\frac{\pi}{4}, 0\}, \{\frac{4\pi}{15}, 0\}, \{\frac{17\pi}{60}, 0\}, \{\frac{3\pi}{10}, 0\}, \{\frac{19\pi}{60}, 0\}, \{\frac{\pi}{3}, 0\}, \{\frac{7\pi}{20}, 0\}, \{\frac{11\pi}{30}, 0\}, \{\frac{23\pi}{60}, 0\}, \{\frac{2\pi}{5}, 0\}, \{\frac{5\pi}{12}, 0\}, \{\frac{13\pi}{30}, 0\}, \{\frac{9\pi}{20}, 0\}, \{\frac{7\pi}{15}, 0\}, \{\frac{29\pi}{60}, 0\}, \{\frac{\pi}{2}, 0\}\}$$

```
ListPlot[MM3, PlotJoined → True, AxesLabel → TraditionalForm /@ {θ, P (θ)},
  TextStyle → {FontFamily → "Times", FontSize → 14}, PlotStyle → {Hue[0.85]}]
```

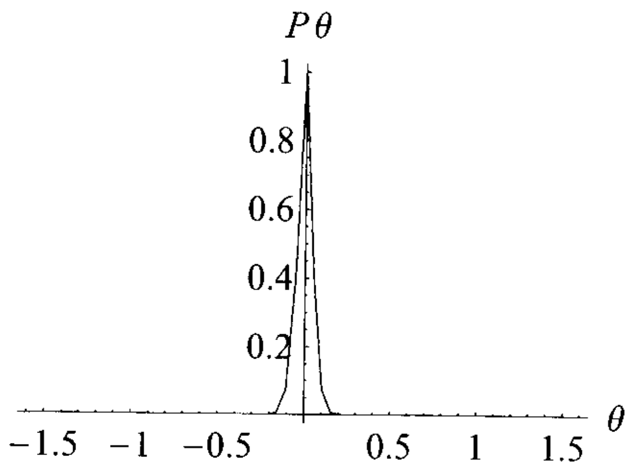

- Graphics -